

Cooperation between Caenorhabditis elegans COMPASS and condensin in germline chromatin organization

Marion Herbette

Ecole Normale Supérieure de Lyon, Université de Lyon

Valérie Robert

Ecole Normale Supérieure de Lyon, Université de Lyon

Aymeric Bailly

CRBM, University of Montpellier

Loïc Gely

Ecole Normale Supérieure de Lyon

Robert Feil

Institute of Molecular Genetics of Montpellier, University of Montpellier

David Llères

University of Montpellier

Francesca Palladino (✉ francesca.palladino@ens-lyon.fr)

Ecole normale supérieure de Lyon <https://orcid.org/0000-0003-3087-449X>

Research

Keywords: COMPASS, SET1, FLIM-FRET, condensin, topoisomerase, C. elegans, meiosis

Posted Date: March 17th, 2020

DOI: <https://doi.org/10.21203/rs.3.rs-17459/v1>

License: © ⓘ This work is licensed under a Creative Commons Attribution 4.0 International License.

[Read Full License](#)

1 **Cooperation between *Caenorhabditis elegans* COMPASS and condensin in germline chromatin**
2 **organization**

3 M. Herbet¹, V. Robert¹, A. Bailly², L. Gely¹, R. Feil³, D. Llères^{3,4} and F. Palladino^{1,4}

4 ¹Laboratory of Biology and Modeling of the Cell, UMR5239 CNRS/Ecole Normale Supérieure de Lyon,
5 INSERM U1210, UMS 3444 Biosciences Lyon Gerland, Université de Lyon, Lyon, France.

6 ²CRBM, University of Montpellier, CNRS, France.

7 ³Institute of Molecular Genetics of Montpellier (IGMM), CNRS, University of Montpellier,
8 Montpellier, France.

9 ⁴corresponding author

10

11 **Abstract**

12 **Background**

13 Histone-modifying activities play important roles in gene expression and influence higher-order
14 genome organization. SET1/COMPASS (Complex Proteins Associated with Set1) deposits
15 histone H3 lysine 4 (H3K4) methylation at promoter regions and is associated with context-dependent
16 effects on gene expression. Whether it also contributes to higher-order chromosome organization has
17 not been explored.

18 **Results**

19 Using a quantitative FRET (Förster resonance energy transfer)-based fluorescence lifetime imaging
20 microscopy (FLIM) approach to assay nanometer scale chromatin compaction in live animals, we reveal
21 a novel role for SET1/COMPASS in structuring meiotic chromosomes in the *C. elegans* germline.
22 Inactivation of SET-2, the *C. elegans* homologue of SET1, strongly enhanced chromosome organization
23 defects and loss of fertility resulting from depletion of condensin-II, and aggravated defects in
24 chromosome morphology resulting from inactivation of topoisomerase II, another major structural
25 component of chromosomes. Loss of CFP-1, the chromatin targeting subunit of COMPASS, similarly
26 affected germline chromatin compaction measured by FLIM-FRET and enhanced condensin-II knock-
27 down phenotypes.

28 **Conclusions**

29 The data presented here are consistent with a role of SET1/COMPASS in shaping meiotic chromosomes
30 in the *C. elegans* germline. This new insight has important implications for how chromatin-modifying
31 complexes and histone modifications may cooperate with non histone-proteins to achieve proper
32 chromosome organization, not only in meiosis, but also in mitosis.

33

34 COMPASS, SET1, FLIM-FRET, condensin, topoisomerase, *C. elegans*, meiosis

35

36 **Background**

37 In different species from yeast to mammals, chromatin modifying complexes and histone post-
38 translational modifications (PTMs) contribute to higher-order chromatin structure (1). While the spatial
39 configuration of chromatin has been shown to be essential to ensure fundamental processes from gene
40 expression to cell divisions, how such higher-order structures are formed in various cellular processes
41 remains unclear. Mitosis and meiosis, two essential processes that require restructuring and
42 reorganization of chromatin architecture, are associated with specific changes in histone modifications.
43 During mitosis, extensive compaction of chromatin is associated with histone H3 serine 10
44 phosphorylation (H3S10ph), H4K20 monomethylation (H4K20me1), and a dramatic reduction in
45 overall histone acetylation (2-4). Specific histone PTMs, including H3K4 tri-methylation (H3K4me3),
46 are also associated with meiotic double strand breaks (DSBs) during recombination, and are dynamically
47 altered during meiotic progression (5-8).

48 The SET1 class of histone methyltransferases act in large multi-subunit complexes known as
49 COMPASS (9,10) to deposit H3K4me3 at promoters of actively transcribed genes. At promoters, levels
50 of COMPASS-dependent H3K4 methylation correlate with transcription levels, but evidence for an
51 instructive role for H3K4me3 in transcription is lacking, and recent data suggest that its role depends on
52 different chromatin and cellular contexts (11).

53 One well-characterized function of H3K4 methylation relies on the binding of effector proteins
54 to mediate downstream processes related to transcription (12-15). Recent data suggest that H3K4me3
55 may also play a more direct role in specific aspects of chromatin organization. For instance, genome-
56 wide changes in H3K4 methylation are observed during mammalian spermatogenesis (16), with a large
57 fraction of dynamic H3K4me3 not coinciding with gene promoters or double strand break (DSB). In
58 mouse oocytes, H3K4 methylation defines distinct nanoscale compartments associated with active
59 transcription that contribute to the shaping of meiotic chromosomes (17).

60 Additional evidence linking SET1/COMPASS to higher-order chromosome organization comes
61 from studies of individual subunits of the complex. For example, in mouse absence of the COMPASS
62 targeting subunit CFP1 results in defects in meiotic oocyte maturation, defective spindle assembly and
63 chromosome misalignment, with only minor effects on transcription (18). In fission yeast, SET1 plays

64 both H3K4-dependent and -independent roles in genome organization through long-range clustering of
65 retrotransposon loci (19-21).

66 *C. elegans* contains a single SET1 homolog encoded by *set-2* (22,23). *set-2* inactivation results
67 in defective patterns of H3K4me3 in the germline and progressive misregulation of the germline
68 transcriptome, leading to increased genome instability and sterility (22–25). Whether these effects
69 reflect a direct role in transcription, or a more general role in germline chromatin organization is not
70 known. Significantly, we previously found no correlation between COMPASS dependent H3K4me3 at
71 promoters and transcription in *C. elegans* embryos, consistent with recent observations in other
72 organisms (26-30). Likewise, increased genome instability in *set-2* mutant germlines was not associated
73 with defects in the induction of the DNA damage response (DDR) pathway, suggesting downstream
74 effects in the DNA repair process (24).

75 In this study, we used fluorescence lifetime imaging microscopy (FLIM) for Förster Resonance
76 Energy Transfer (FRET) measurements in live animals to assess close proximity between nucleosomes
77 and to quantify different levels of chromatin compaction. In meiotic cells from animals lacking
78 COMPASS components SET-2 and CFP-1, we find that FRET between fluorophore-tagged
79 nucleosomes is dramatically decreased, consistent with a structural role for COMPASS affecting
80 nucleosome proximity in the nucleus. In support of such a role, we find that loss of either *set-2* or *cfp-1*
81 enhances the chromosome organization defects resulting from reduced expression of condensin-II, a
82 major contributor to chromosome structure (31). Cooperation between SET-2 and condensin-II in the
83 germline was independently confirmed in animals carrying a temperature-sensitive allele of the
84 condensin-II subunit *hcp-6*. We further show that *set-2* inactivation aggravates the germline phenotypes
85 resulting from conditional inactivation of topoisomerase II, another major component of chromosomes
86 (32). Altogether, our results indicate that COMPASS contributes to the organization of germline
87 chromosome architecture in cooperation with condensin, and have wider implications on the role of
88 COMPASS-related complexes and H3K4 methylation in higher-order chromatin structure.

89

90 **Results**

91 **Nanoscale chromatin compaction is decreased in *set-2* mutant germlines**

92 In the *C. elegans* germline, meiotic nuclei are arranged in a temporal-spatial order, with the distal end
93 of the gonad containing mitotically proliferating nuclei. Homolog pairing initiates downstream in the
94 “transition zone”, followed by pachytene, during which synapsed chromosomes appear in DAPI-stained
95 nuclei as discrete, parallel tracks. More proximally, nuclei exit pachytene, enter diplotene, and
96 cellularized oocytes containing condensed homologs are formed (33).

97 H3K4me3 is detected on chromatin in all germline nuclei, from the distal mitotic region through
98 the meiotic stages and into diakinesis (Figure S1A)(22,23). In germlines from animals carrying the *set-*
99 *2(bn129)* loss-of-function frameshift allele that results in a premature stop codon (22), H3K4me3
100 strongly decreases in the distal mitotic region through early-mid pachytene. Levels of H3K4me3 are not
101 visibly altered in late pachytene and diakinetin nuclei of mutant animals, most likely reflecting the
102 additional activity of SET-16/MLL, the only other SET1 family member in *C. elegans* (Figure S1A,
103 (22,23,34,35). Reduced H3K4 methylation in *set-2(bn129)* animals is associated with a progressive
104 decrease in fertility at the stressful temperature of 25°C, resulting in sterility at the F4-F5 generation
105 (22,23). These observations suggest that H3K4 methylation, or SET 2 itself, play an important role in
106 germline maintenance. DAPI staining of chromatin revealed no apparent defects in either germline
107 organization, or chromosome morphology in *set-2* mutant animals raised under normal conditions
108 (20°C), or late generation fertile animals at 25°C (data not shown and (22). Interestingly however, in
109 late generation (F4) germline nuclei from animals approaching sterility at 25°C, chromatin appeared
110 less organized than in wildtype animals, with a loss of the distinctive pachytene nuclei morphology
111 (Figure S1B). These results suggest that SET-2 may have an impact on global genome organization.

112 Chromatin modifying complexes and histone modifications define the different functional states
113 of chromatin throughout the genome, and these in turn contribute to higher-order chromatin organization
114 (36). To investigate whether and how COMPASS influences higher-order chromatin compaction
115 specifically in germline cells, we used a recently developed FLIM-FRET technique that enables
116 quantification of chromatin condensation levels in live animals at the level of nucleosome packaging.
117 The assay is based on the measurement of FRET interaction between fluorescently-labelled core histone
118 GFP::H2B (donor) and mCherry::H2B (acceptor) co-expressed in the *C. elegans* germline (37).
119 Importantly, FRET is a phenomenon sensitive to fluorophore proximity that occurs efficiently only when

120 the donor and acceptor fluorescent fusion proteins are closely positioned (<10nm) in the 3D nuclear
121 space following chromatin compaction. By measuring histone-histone proximity, this FRET assay can
122 respond to changes in nucleosome spacing, and therefore provides a read-out of nanoscale chromatin
123 compaction (38-41). FLIM-FRET also provides accurate quantification due to the independence of the
124 fluorescence lifetime from the relative concentrations of the interacting proteins, and is independent of
125 their diffusion rates (42). To carry out the assay, we first generated wildtype and *set-2* mutant strains
126 that stably co-express both GFP-H2B and mCherry-H2B fusion proteins (FPs, named “H2B-2FPs”
127 hereafter) from a single transcription unit driven by the germline-specific *pmex-5* promoter (Figure 1A).
128 We confirmed that there was no alteration in the expression of fluorescent-tagged H2B histones in *set-*
129 *2* mutants (Figure S2A), and fluorescence recovery after photo-bleaching (FRAP) showed that tagged
130 histones H2B were stably incorporated into chromatin in *set-2* mutants (Figure S2B).

131 Comparative FLIM-FRET analysis of *set-2(bn129)*H2B-2FPs and wth2B-2FPs pachytene nuclei
132 revealed a strong reduction in chromatin compaction levels in the absence of *set-2*, as indicated by a
133 longer GFP-H2B fluorescence lifetime (Figure 1A), and a reduced mean-FRET efficiency (Figure 1B).
134 Quantification of FRET efficiencies in individual nuclei allowed us to arbitrarily define several classes
135 of FRET, from “sub-low FRET” to “high-FRET”, as previously described (43). Interestingly, we
136 observed that in the absence of *set-2*, “intermediate-FRET” and “high-FRET” populations previously
137 linked to heterochromatic states (43) were significantly reduced compared to wild type (Figure 1C),
138 while the “sub-low-FRET” chromatin class associated with more accessible chromatin was increased.
139 These results suggest that the absence of SET-2 influences nanoscale chromatin structure in the
140 germline.

141 **Loss of *set-2* enhances chromosome organization defects resulting from condensin-II knock-down**

142 If SET-2 contributes to chromatin organization in germ cells, one prediction is that its absence might
143 impact chromosome function and result in chromosome segregation defects in meiosis, thereby
144 generating aneuploid cells (44). We found no evidence for such defects in *set-2* mutant animals (24, 30,
145 45). What we did find, however, is that endoreplicated intestinal cells of adult animals showed
146 chromosome segregation defects very similar to those reported in condensin-II mutants (45,46). This
147 raised the possibility that in normally dividing cells of these mutants, more subtle defects in germline

148 chromatin organization arise that become clearly apparent only in a sensitized background in which
149 chromatin structure is further perturbed.

150 Condensins are major contributors to chromosome structure and organization (31). Metazoans
151 contain two types of condensin complexes (I and II) that share a heterodimer of two 'structural
152 maintenance of chromosomes' (SMC) proteins, SMC2 and SMC4, and are distinguished by three unique
153 CAP (chromosome-associated polypeptide) proteins named CAPG, CAPD and CAPH (47). Uniquely,
154 *C. elegans* has an additional complex, condensin-IDC, which contributes exclusively to dosage
155 compensation in somatic cells (48). KLE-2, HCP-6 and CAPG-2 are condensin-II specific subunits,
156 CAPG-1, DPY-26 and DPY-28 are common to the two condensin-I complexes, whereas DPY-27 is
157 specific to condensin-IDC (Figure 2A) (46). In *C. elegans*, condensin-II associates with sister chromatids
158 in meiosis and mediates their compaction and resolution (49, 50). Because depletion of condensin-II
159 subunits results in sterility, we could not study the interaction of single condensin-II mutants with *set-*
160 *2*. Instead, we knocked-down different subunits of condensin in wildtype and *set-2* mutant animals by
161 growing animals from the L1 larval stage to adulthood on condensin RNAi feeding plates, followed by
162 scoring of DAPI stained germlines by fluorescence microscopy (Figure 2B and D). We first focused on
163 *kle-2* and *capg-1* RNAi to knock-down condensin-II and condensin-I complexes, respectively. RT-
164 qPCR analysis showed that RNAi treatments resulted in a similar decrease in transcript levels in both
165 wildtype and *set-2* mutant animals (Figure 2C), confirming that the efficiency of RNAi was the same in
166 both contexts.

167 Condensin-II RNAi resulted in partial sterility in both wildtype and mutant animals. Because
168 many of these animals also showed somatic defects that prevented egg-laying, we were unable to use
169 the number of progeny laid as a read-out of fertility in these experiments. We instead turned to visual
170 scoring of germlines, placing animals in one of two broad classes: "wildtype-like" or "abnormal"
171 (Figures 2B and D). Germlines in the wildtype-like class consisted of nuclei undergoing all stages of
172 meiotic progression as in wild type, although the total number of germ cells was reduced, consistent
173 with the severe under-proliferation observed in condensin-II mutants (46). The second class defined as
174 "abnormal" consisted of severely disorganized germlines containing fewer and larger nuclei, often

175 showing more intense DAPI staining (Figure 2B and D). Using a lacO/lacI-GFP system composed of a
176 stably integrated lacO array and a lacI::GFP fusion protein able to bind LacO repeats (51), we observed
177 multiple spots in enlarged nuclei, revealing that these were aneuploid nuclei (Figure S3). The abnormal
178 germline morphology of these mutants made it difficult to clearly distinguish different region of the
179 germline, and individual cells could not be unequivocally assigned to a specific meiotic stages. Nuclei
180 were sometimes connected by thin chromatin bridges (Figure 2B, arrow), consistent with the known
181 involvement of condensin-II in chromosome segregation in the germline and soma (46)(52).

182 RNAi of the condensin-II subunit *kle-2* in wildtype animals resulted in an equal number of
183 germlines falling in the wildtype-like and abnormal class (Figure 2B). *kle-2*(RNAi) in *set-2* mutant
184 animals resulted in similar phenotypes, but the number of germlines showing an abnormal phenotype
185 was significantly higher, representing 80% of all germlines in blind scoring experiments. Similar results
186 were observed following RNAi knock-down of the other condensin-II specific subunits, *hcp-6* and *capg-*
187 *2*, as well as *smc-4*, common to both condensin I and II complexes. In all conditions, phenotypes were
188 consistently and significantly more severe in *set-2* mutant animals than in wildtype animals (Figure 2D).
189 Knockdown of the condensin-I specific subunits *capg-1* and *dpy-28*, or the condensin-Idc subunit *dpy-*
190 *27*, did not produce any apparent germline phenotype, either alone, or in the *set-2* mutant background
191 (Figure 2D) (46,49,50). The effectiveness of *capg-1*, *dpy-28* and *dpy-27* RNAi was confirmed by scoring
192 the associated dumpy (Dpy) phenotype in wildtype and mutant animals (Figure S4;
193 www.wormbase.com). In summary, germline phenotypes resulting from condensin-II knock-down are
194 significantly and reproducibly more severe in the absence of *set-2*, and these marked defects are not
195 observed following knock-down of the other two condensin complexes in *C. elegans*. Importantly,
196 transcriptome profiling of *set-2* mutant germlines did not show mis-regulation of condensin subunits, or
197 of other genes with obvious functions in chromosome organization, further supporting a transcription-
198 independent effect (Table S1). Altogether, these results strongly suggest that *set-2* contributes to proper
199 meiotic chromosome organization in the *C. elegans* germline, a process largely dependent on condensin-
200 II activity.

201 **Increased sterility and germline apoptosis in *hcp-6(mr17);set-2* double mutants**

202 To validate the above results based on RNAi knock-down, we used *mr17*, a hypomorphic allele of the
203 condensin-II subunit *hcp-6* that carries a missense mutation resulting in temperature-sensitive
204 embryonic lethality (52). In their previous analysis, the authors identified it as a G to A transition at
205 nucleotide position 3073 within the coding region, converting glycine 1024 to glutamic acid (52). We
206 could not confirm the identity of this mutation by resequencing. Instead, we identified a glycine to
207 glutamic acid substitution at amino acid 683 within the HEAT repeat of HCP-6 (Figure 3A).

208 Because the germlines of *hcp-6(mr17)* single and double mutants are severely disorganized at
209 25°C (Figure S5 A), we were unable to visually score distinct phenotypic classes in single compared to
210 *hcp-6(mr17);set-2* double mutants, as we did for the RNAi experiments. However, we observed that
211 *hcp-6(mr17)* mutants showed a significant reduction in the number of progeny laid at all temperatures
212 tested (15°, 20°, 25°C) (Figure 3B), consistent with the essential role of condensin-II in germline fertility
213 (46). Using total brood size as a read-out of germline health, we found that *set-2* single mutants laid
214 fewer eggs at all temperatures tested, as previously described (22). Brood size was further and
215 significantly reduced in *hcp-6(mr17);set-2* double mutants compared to either of the single mutants at
216 all temperatures (Figure 3B). Furthermore, in all cases, the *hcp-6(mr17);set-2* double mutant phenotype
217 was most severe at the non-permissive temperature of 25°C. *hcp-6(mr17);set-2* double mutants laid a
218 mean of 30 embryos per animal at 25°C, compared to 250-300 for wild type, showing that germline
219 function was severely impacted in these animals.

220 Defective germline nuclei in *C. elegans* hermaphrodites are eliminated by apoptosis (53,54),
221 which could contribute to the reduced brood size of *hcp-6* mutant animals. Using the dye acridine orange
222 as a marker of apoptotic cells (53), we observed as expected an increase in apoptosis in *brc-1/BRCA1*
223 mutants (55), while *set-2* single mutants were unaffected, as previously shown (Figures 3C and D)(24).
224 The number of apoptotic corpses was increased in *hcp-6* mutants, with a significant further increase in
225 *set-2;hcp-6(mr17)* double mutants. The elimination of defective germline nuclei by apoptosis may
226 therefore contribute to the reduced fertility of these animals. Alternative, or in addition, a decrease in
227 the mitotic stem cell population may contribute to the observed reduction in brood size. Altogether, our
228 results are consistent with RNAi knock-down experiments and suggest that condensin-II and *set-2* may
229 act in similar processes in the germline.

230 The *hcp-6(mr17)* allele also offered the opportunity to ask whether *set-2* genetically interacts
231 with condensin-II in embryos. To test this possibility, L4 animals raised at the permissive temperature
232 of 15°C were shifted to 20°C and allowed to develop into adults, followed by scoring of their progeny.
233 Under these conditions, *hcp-6(mr17)* animals showed more than 85% embryonic lethality (Figure S5
234 B). Surprisingly, we observed that embryonic lethality was significantly reduced to 65% in *set-2;hcp-*
235 *6(mr17)* double mutants (Figure S5 B). Animals that hatched developed into adults showing phenotypes
236 associated with cell division defects, including uncoordinated behaviour and sterility (56), suggesting
237 that partial suppression of embryonic lethality in the absence of *set-2* may be independent of an effect
238 on chromosome segregation. Altogether, these results support the hypothesis of a functional interaction
239 of *set-2* with condensin-II in both the germline and embryos.

240 ***set-2* inactivation also enhances chromosome organization defects of *top-2(it7)* mutant germlines**

241 In addition to condensin complexes, topoisomerase II is another major component of mitotic
242 chromosomes. Functional loss of topoisomerase II leads to defects in chromosome morphology and
243 abnormal mitotic chromosome segregation in all species studied (57–59), including *C. elegans* (60).
244 When temperature-sensitive topoisomerase II mutants are used to bypass its essential requirement in
245 mitosis, defects in chromosome condensation and segregation are also observed in meiosis (61-64).
246 TOP-2, the single *C. elegans* topoisomerase II, shows linear localization along the exterior of mitotic
247 chromosomes, consistent with a structural role (60). To test whether *top-2* interacts with *set-2* to ensure
248 proper chromosome condensation in the germline, we constructed *set-2;top-2* double mutants using a
249 recently described allele, *top-2(it7)*, that was shown to result in a temperature-sensitive chromosome
250 segregation defect in male spermatogenesis (65).

251 We observed that *top-2(it7)* hermaphrodites that developed from animals shifted to the non-
252 permissive temperature (24°C) at the L1 larval stage also had defects in germline organization.
253 Approximately one third (36%) of adults contained normal germline arms whose size and developmental
254 transitions were comparable to wild type (Figure 4A). The remaining animals contained either a smaller
255 germline, such that germline bends were premature, or a germline atrophy phenotype with only a small
256 population of mitotic germ cells. Notably, animals that displayed germline atrophy were mostly devoid
257 of germ cells at various stages of meiosis (66). Atrophied germlines were significantly more abundant

258 in *top-2(it7);set-2* double than in *top-2* single mutants, accounting for 65% of all germlines scored
259 (n=400) (Figure 4A). In addition, we observed a minor fraction of germlines consisting of only mitotic
260 germ cells (tumorous phenotype, data not shown). Altogether, these results show that the combined
261 absence of *top-2* and *set-2* results in a dramatic germ cell atrophy.

262 In wildtype oocytes, individual chromosomes appear as 6 condensed DAPI stained structures
263 (33). Consistent with the established role of topoisomerase II in sister chromatid segregation (59,67–
264 71), *top-2(it7)* mutants had a significant number of oocytes (33%) with more than 6 DAPI-stained bodies
265 (Figure 4C and D). A similar phenotype was observed in *top-2(it7);set-2* double mutants, suggesting
266 that this particular function of topoisomerase II is independent of SET-2. Altogether, these results are
267 consistent with a role for SET-2 in cooperation with condensin and Topo II, two major components of
268 chromosome architecture, to achieve proper chromatin organization of pachytene chromosomes.

269 **Loss of COMPASS targeting subunit CFP-1 results in similar chromatin organization defects as** 270 **SET-2 inactivation**

271 We next asked whether other subunits of COMPASS also enhance the germline defects resulting from
272 condensin-II knockdown. As observed for *set-2*, inactivation of *cfp-1* using either the deletion allele
273 *tm6369* or RNAi resulted in a strong decrease in H3K4me3 in both the germline and soma (22,72,73
274 and Figure S6 A). The number of animals with an abnormal germline phenotype following RNAi of
275 *smc-4*, targeting condensin-I and -II, or *kle-2*, targeting condensin-II only, was largely increased in *cfp-1*
276 mutants compared to wild type (Figure 5A). FLIM-FRET analysis of *cfp-1* mutants expressing H2B-
277 2FP showed a drastic nanoscale decompaction of pachytene chromatin (Figure 5B), further supporting
278 a role for COMPASS in chromosome organization.

279 As in other species, H3K4me3 in *C. elegans* is removed by the well-conserved lysine
280 demethylase RBR-2/KDM5, and H3K4me3 levels are strongly increased in its absence at all
281 developmental stages (74-76). *rbr-2* has been shown to counteract the effect of COMPASS on longevity
282 (77), but like *set-2* is required to maintain germline immortality at high temperatures (75). We found
283 that absence of RBR-2 activity in the *rbr-2(tm1231)* deletion allele (75) did not result in enhancement
284 of germline defects resulting from either *kle-2* or *smc-4* (RNAi) (Figure 5A). qRT-PCR analysis
285 confirmed that although the overall efficacy of RNAi varied between independent experiments (78),

286 within the same experiment efficacy was comparable in wildtype, *cfp-1* and *rbr-2* mutants (Figure S6
287 B). Furthermore, the percentage of animals with a strong phenotype was similar in all three experiments
288 (Figure S6 C), consistent with depletion of condensin-II below a threshold level being sufficient to
289 provoke defects in chromosome organization (81). Therefore, contrary to COMPASS inactivation,
290 increasing H3K4 methylation levels in *rbr-2* mutants has no obvious impact on germline chromatin
291 organization.

292

293 **Discussion**

294 Using three different experimental approaches, we show that in the *C. elegans* germline the COMPASS
295 H3K4 methyltransferase complex contributes to the organization of chromosome architecture. First,
296 using quantitative FLIM-FRET we found that chromatin compaction is affected at the nucleosomal level
297 in live animals that lack the COMPASS subunits SET-2 and CFP-1. Second, we demonstrate that defects
298 in germline nuclei compaction following RNAi knock-down of condensin-II subunits are strongly
299 enhanced in the absence of either SET-2 or CFP-1. Third, using the number of progeny as a read-out of
300 fertility, we found that *set-2* inactivation exacerbates the fertility defects associated with a hypomorphic
301 allele of the condensin-II subunit *hcp-6*.

302 A current model proposes that condensin complexes topologically shape mitotic chromosomes
303 through a loop extrusion process (79), with condensin-I and -II forming arrays of helical consecutive
304 loops in mitotic cells (80). However, the fact that chromosomes still maintain a certain degree of
305 structure in the absence of both condensin-I and -II suggests that additional mechanisms and factors,
306 including histone modifying complexes and the associated modifications, may also be involved (4,81-
307 85,87). Using the same FLIM-FRET imaging approach as implemented here, we previously showed that
308 condensin complexes contribute to the nanoscale compaction of chromatin in the *C. elegans* germline
309 (43). Depletion of condensin-I affected both highly and lowly compacted regions, whereas depletion of
310 condensin-II only affected highly compacted regions (43). Here, by quantifying nucleosomes proximity
311 using FRET imaging, we observed that the absence of *set-2* affects the same compacted chromatin states
312 as the condensin-I complex (43). This suggests that *set-2*, and to a larger extent COMPASS as a whole,

313 may contribute to the formation of loops to establish the proper structural organization of meiotic
314 chromosomes.

315 Because complete inactivation of condensin-II resulted in chromosome segregation defects and
316 embryonic lethality, we used RNAi to look at the effect of mild depletion of condensin-II in the absence
317 of COMPASS subunits. In mammals, partial inactivation of condensin by a similar approach was also
318 shown to result in relatively moderate defects in chromosome structure (47,87-90). Our data show that
319 mild depletion of condensins in *C. elegans* results in less compacted pachytene chromosomes, and that
320 the absence of COMPASS subunits *set-2* or *cfp-1* significantly aggravates this defect. We further
321 confirmed that COMPASS and condensin-II functionally cooperate in the germline by showing that the
322 reduced fertility of the hypomorphic allele *hcp-6(mr17)* is aggravated in the absence of *set-2*. By
323 resequencing the *hcp-6(mr17)* allele, we identified the mutation as a substitution of glycine with
324 glutamic acid within one of the α -helical HEAT repeats of HCP-6. Although the role of the HEAT-
325 repeat subunits, which are unique to eukaryotic condensins, remains largely unknown (91), our results
326 suggest that they are of functional importance.

327 Interestingly, we also found that *set-2* partially suppressed the embryonic lethality of *hcp-*
328 *6(mr17)* mutants at the non-permissive temperature. Our data suggest that increased apoptosis in *set-*
329 *2;hcp-6* double mutant germlines may eliminate defective germ cells, thereby improving the quality of
330 surviving oocytes with respect to the *hcp-6* single mutant. Consistent with this model, increased
331 apoptosis has also been observed in the germline of condensin-I deficient worms (92). Interestingly
332 mutations in the BRCA1 homologs *brc-1* or *brd-1* are also able to partially suppress the embryonic
333 lethality of *hcp-6*(RNAi) animals, possibly reflecting a role for BRC-1/BRD-1 in the formation of toxic
334 chromatin bridges when chromosome condensation is defective (93). Our results suggest that SET-2
335 may also be involved in a similar process in embryos.

336 The observation that *set-2* inactivation also enhances the defects in chromatin organization of
337 *top-2* conditional mutants further supports a structural role for SET-2 in higher-order chromatin
338 organization. Topo II and condensin are both major components of the proteinaceous mitotic scaffold
339 from which radial chromatin loops radiate (94,95), and Topo II contributes to proper mitotic
340 condensation and structure in various organisms (59,81,96–103). In *C. elegans*, TOP-2 localizes along

341 the chromosome length in mitosis and has been proposed to constrain chromosome length by modulating
342 chromatin loops (60). As in mitosis, topoisomerase II localizes along the chromosome axes of meiosis
343 I chromosomes in yeast and mammals (62,63,104), suggesting that it may play a similar structural role
344 in organizing *C. elegans* germline nuclei.

345 How might COMPASS contribute to the higher order organization of chromosomes in the *C.*
346 *elegans* germline? Our transcriptomic analysis of *set-2* depleted germ cells reveals only minor
347 transcriptional changes (Figure S1), suggestive of a structural role rather than an indirect transcriptional
348 effect. Likewise, inactivation of the SETD1–CFP1 complex in mouse oocytes results in chromosome
349 organization defects independent of transcription (18,105). We also consider a direct effect of SET-2 on
350 condensin-II unlikely, since we found no evidence of a direct physical interaction between the two
351 proteins in extensive proteomics analysis ((30) and data not shown). Rather, the enhancement of
352 condensin-II knock-down phenotypes by COMPASS inactivation suggests at least partially
353 independent, cumulative, effects on chromosome organization (Figure 6). Meiotic chromosomes from
354 yeast to mammals are organized as linear loop arrays around a proteinaceous chromosome axis (106–
355 109), and recent super-resolution microscopy studies on mouse oocytes show that H3K4me3 emanates
356 radially in similar structures (17). In mouse spermatocytes, strong clustering of highly transcribed loci
357 is observed and is thought to be the result of interactions occurring locally between linear loops, as well
358 as between loci on homologs (110). Based on these observations, we suggest that the presence of
359 COMPASS at transcription sites could contribute to the organization of chromatin in these clusters. This
360 could take place through the recruitment of an H3K4me3 reader, as described for the NCAPD3 subunit
361 of condensin-II (111), or through the recruitment of additional proteins (30). Finally, given the recent
362 implication of the nuclear RNAi pathway and the MORC-1 gene silencing protein in germline chromatin
363 organization (112,113), additional interactions between COMPASS and these pathways may be
364 involved. Deciphering the mechanism whereby chromatin-associated factors and histone post-
365 translational modifications affect global regulation of chromatin architecture in meiosis will be an
366 important area of future study.

367 **Conclusions**

368 Our studies highlight a novel role for SET1/COMPASS in chromosome organization in the *C. elegans*
369 germline. Given the remarkable morphological similarities between chromosomes in meiotic prophase
370 and early mitotic prophase (80,114–1119), our germline findings may have implications for mitotic
371 chromosome condensation as well.

372

373 **Methods**

374 **Nematode maintenance and strains**

375 Unless otherwise noted, animals were propagated under standard conditions at 20°C or 15°C (120) on
376 NGM plates (Nematode Growth Medium) seeded with the *Escherichia coli* strains OP50 or HT115 for
377 RNAi experiments. N2 bristol was used as the wildtype control strain. Strains used were as follows:

378 *hcp-6(mr17)* I (PFR656), *set-2(bn129)* III/qC1 (PFR510), *hcp-6(mr17)* I; *set-2(bn129)* III (PFR651),
379 *cfp-1(tm6369)* IV (PFR588), *brc-1(tm1145)* III (DW102), *rbr-2(tm1231)* IV (PFR394), *oxIs279[Ppie*
380 *1::GFP::H2B + unc-119(+)]* II; *unc-119(ed3)* III (EG4601), *oxIs279[Ppie-1::GFP::H2B + unc-119(+)]*
381 *II; set-2(bn129)* III (PFR326), *oxIs279[Ppie-1::GFP::H2B + unc-119(+)]* II; *cfp-1(tm6369)* IV
382 (PFR667), *oxSi487 [mex-5p::mCherry::H2B::tbb-2 3'UTR::gpd-2 operon::GFP::H2B::cye-1 3'UTR +*
383 *unc-119(+)]* II; *unc-119(ed3)* III (EG6787), *oxSi487 [mex-5p::mCherry::H2B::tbb-2 3'UTR::gpd-2*
384 *operon::GFP::H2B::cye-1 3'UTR + unc-119(+)]* II; *set-2(bn129)* III (PFR659), *oxSi487 [mex-*
385 *5p::mCherry::H2B::tbb-2 3'UTR::gpd-2 operon::GFP::H2B::cye-1 3'UTR + unc-119(+)]* II; *cfp-*
386 *1(tm6369)* IV (PFR666), *unc-119(ed3)* III; *top-2(it7)* II (PFR704), *top-2(it7)* II; *set-2(bn129)* III
387 (PFR705)

388 **Worm Live-Imaging Preparation**

389 For FRAP and FLIM-FRET acquisitions, single worms (24 hours post-L4 stage) from an
390 unsynchronized population were picked to an unseeded 1xNGM plate to wash off bacteria and were
391 subsequently transferred onto a glass slide in a drop of egg buffer (118 mM NaCl, 48 mM KCl, 2 mM
392 CaCl₂*2H₂O, 2 mM MgCl₂*6H₂O, 25 mM HEPES pH 7.3). Worm gonads were extruded by
393 microdissection using a 23G syringe and immediately covered with a coverslip, sealed with nail varnish.

394 **FLIM-FRET Acquisition**

395 FLIM-FRET measurements were carried out on wt, *set-2(bn129)* and *cfp-1(tm6369)* mutant strains
396 GFP-H2B (donor alone: GFP-H2B protein) and H2B-2FPs (donor and acceptor: GFP-H2B and
397 mCherry-H2B). FLIM was performed using an inverted laser scanning multi-photon LSM780
398 microscope (Zeiss) equipped with an environmental black-walled chamber. Measurements were
399 performed at 20°C with a 40x oil immersion lens, NA 1.3 Plan-Apochromat objective, from Zeiss. Two-
400 photon excitation was achieved using a tunable Chameleon Ultra II (680–1,080 nm) laser (Coherent) to
401 pump a mode-locked, frequency-doubled Ti:sapphire laser that provided sub-150-fs pulses at an 80-
402 MHz repetition rate. GFP and mCherry fluorophores were used as a FRET pair. The optimal two-photon
403 excitation wavelength to excite the donor GFP was determined to be 890 nm (37). Laser power was
404 adjusted to give a mean photon count rate of about $7 \cdot 10^4$ – 10^5 photons per second. Fluorescence lifetime
405 measurements were acquired over 60 s. Detection of the emitted photons was achieved through the use
406 of an HPM-100 module (Hamamatsu R10467-40 GaAsP hybrid photomultiplier tube [PMT]). and
407 fluorescence lifetimes were calculated for all pixels in the field of view (256 x 256 pixels). The
408 fluorescence lifetime imaging capability was provided by time-correlated single- photon counting
409 (TCSPC) electronics (SPC-830; Becker & Hickl). TCSPC measures the time elapsed between laser
410 pulses and the fluorescence photons. Specific regions of interest (e.g., full gonad or pachytene nuclei)
411 were selected using SPCImage software (Becker & Hickl).

412 **FLIM-FRET Analysis**

413 FLIM measurements were analyzed as described previously (43) using SPCImage software (Becker &
414 Hickl). Briefly, FRET results from direct interactions between donor and acceptor molecules (121) and
415 causes a decrease in the fluorescence lifetime of the donor molecules (GFP). The FRET efficiency (*i.e.*,
416 coupling efficiency) was calculated by comparing the fluorescence lifetime values from FLIM
417 measurements obtained for GFP donor fluorophores in the presence and absence of mCherry acceptor
418 fluorophores. The FRET percentage images were calculated such as, $E_{FRET} = 1 - (\tau_{DA}/\tau_D)$, where τ_{DA}
419 is the mean fluorescence lifetime of the donor (GFP-H2B) in the presence of the acceptor (mCherry-
420 H2B) expressed in *C. elegans*_{H2B-2FPs}, and τ_D is the mean fluorescence lifetime of the donor (GFP-H2B)
421 expressed in *C. elegans*_{GFP-H2B} in the absence of the acceptor. In the non-FRET conditions, the mean

422 fluorescence lifetime value of the donor was calculated from a mean of the τ_D by applying a mono-
423 exponential decay model to fit the fluorescence lifetime decays.

424 **Condensin RNAi knockdown**

425 Bacterial clones expressing RNA targeting condensin-I and -II subunit were from the *C. elegans* RNAi
426 collection (Ahringer laboratory-Gene Service Inc). Inserts from each RNAi clone were amplified by
427 PCR on isolated colonies, with a single primer in the duplicated T7 promoter (5'
428 TAATACGACTCACTATAGGG 3'), then sequenced using the primer 5'
429 GGTCGACGGTATCGATAAGC 3'. RNAi clones were cultured in LB liquid medium supplemented
430 with 50 μ g/ml Ampicillin for 18h at 37°C, IPTG was then added (1mM final), and cultures grown an
431 additional 2h30 at 37°C. NGM plates complemented with IPTG (1mM) were seeded with 300 μ l of
432 bacterial culture. Synchronized L1 were placed on RNAi plates and grown to adulthood.

433 **RNA isolation and qRT-PCR analysis**

434 Synchronized L1 wildtype or *set-2(bn129)* mutant worms were grown on empty vector L4440 or *kle-2*
435 or *capg-1* RNAi to adult staged worms at 20°C and harvested. Total RNA was isolated using NucleoZol
436 (Macherey Nagel, #740404-200) and NucleoSpin (Macherey Nagel, #40609). RNA was reverse
437 transcribed using cDNA transcriptor (Roche, #5893151001). Quantitative PCR analysis was performed
438 on CFX Connect (Bio-rad CFX Connect) with SYBR Green RT-PCR (Roche, #4913914001). Melting
439 curve analysis was performed for each primer set to ensure the specificity of the amplified product and
440 with an efficiency of 2. *pmp-3* and *cdc-42* were used as the internal controls so that the RNA level of
441 each gene of interest was normalized to the levels of *pmp-3* and *cdc-42*. qRT-PCR were performed on
442 three biological replicas in technical duplicates. Statistical analysis was performed using an unpaired t-
443 test. Primers used were:

444 *pmp-3*: 5' GTTCCCGTGTTCACTCAT 3' — 5' ACACCGTCGAGAAGCTGTAGA 3'

445 *cdc-42*: 5' CTGCTGGACAGGAAGATTACG 3' — 5' CTCGGACATTCTCGAATGAAG 3'

446 *kle-2*: 5' GAGAAAACGGACAGCTCGTGTG 3' — 5' CGTCATATTCAGCTCCGAGGGT 3'

447 *capg-1*: 5' TCGAATTGGCCAGTAGATGC 3' — 5' ACTGCAACAAGTCGGCATTTC 3'

448 **Hoechst staining on dissected germlines**

449 Germlines from condensin RNAi knock-down animals were dissected on L-polylysine coated slides in
450 a drop of dissection buffer (0.4X M9 and Levamisole 20mM). After removing dissection buffer using a
451 drawn capillary, gonads were fixed in 11µl of 3% paraformaldehyde for 5min. Slides were washed in
452 1X PBS 0.2% Tween 20 plus 5µg/ml Hoechst 33342 (Sigma Aldrich, #861405) for 10 min, then twice
453 in 1X PBS 0.2% Tween 20 for 10 min, and mounted in mounting media (1X PBS, 4% n-Propyl-Gallate,
454 90% DE Glycerol). Z-stack images (0.25 µm slices) of germlines were acquired using a Zeiss LSM710
455 inverted confocal microscope with a 40X oil immersion objective.

456 **DAPI staining on whole animals**

457 For scoring topo II mutant germlines, adult animals were stained as previously described (122) with
458 minor modifications. Briefly, animals were collected and washed once in 1X M9, fixed 15 min in -20°C
459 methanol, and washed twice in 1X PBS with 0.1% Tween 20 (Sigma Aldrich, #P1379). 25µl
460 Fluoroshield plus DAPI (Sigma Aldrich, #F6057) was added directly to 50µl of worm pellet, followed
461 by mounting for fluorescent microscopy. Observation were made on an AxioImager A2 (Zeiss) with
462 Plan Apochromat 63X/1.4 oil DIC or EC plan Neofluar 20X/0.5 objectives.

463 **Scoring of germline phenotypes**

464 Blind scoring was carried out using AxioImager A2 (Zeiss) with EC plan Neofluar 20X/0.5 objectives.
465 For condensin RNAi knock-down, the "strong phenotype" was defined as germlines containing fewer,
466 abnormally sized and unevenly distributed nuclei, as well as macro nuclei with strong DAPI signal, as
467 previously described (46). "weak phenotype" includes wildtype-like germlines that sometimes contained
468 a few macro nuclei with strong DAPI signal. For each experiment, at least 200 germlines were scored
469 for each genotype, and at least 3 independent biological replicates were performed. For experiments
470 with the *top-2(it7)* allele, wildtype, *set-2(bn129)* and *top-2(it7)* single, and *set-2(bn129);top-2(it7)*
471 double mutants were synchronized at the L1 stage at 15°C, then transfer on plates seeded with OP50 at
472 24°C and allowed to develop to adulthood. Adults were recovered in 1X M9 and DAPI stained as
473 described in DAPI staining on whole animals. Germlines were place in phenotypic categories based on
474 (123). Data were collected from 3 independent experiments.

475 **Sequencing and mapping of the *hcp-6(mr17)* mutation**

476 Genomic DNA from wildtype animals (N2) and from strains bearing the *hcp-6(mr17)* mutation was
477 amplified using a high-fidelity polymerase (Phusion®, NEB #M0530S) and the following primer pairs:
478 5' ATAGTCAACCTCGATTGCTGGCTG 3' — 5' GAGGGCGAATAAGTCTTCCGTAAG 3'
479 5' GGAGTTTCTGCTGCCAGTAGTTAT 3' — 5' TGTGGATAAACGTGGCGATA 3'
480 5' GATCGTTGGAGCGATTTACGGATC 3' — 5' TGTGGATAAACGTGGCGATA 3'
481 5' GATCGTTGGAGCGATTTACGGATC 3' — 5' CTTTCTGGCATGTTTCAGTGACGTC 3'
482 5' GAAATCCCGAAGCAAGAGAG 3' — 5' GTCCATGTGAGATCCGATGAGT 3'
483 5' GAAATCCCGAAGCAAGAGAG 3' — 5' CTTTCTGGCATGTTTCAGTGACGTC 3'
484 5' TGGCTTCACACCTTGATCTCGATG 3' — 5' TCTTCATCGTGACCAACTCCAACC 3'
485 5' TCTCAACGTGGCATCTGAAG 3' — 5' GCGTGTCGACGAACAATAAC 3'
486 5' GTTCGGAATGACGCAAAACT 3' — 5' CACAGTTTTCTCCGCATCAACATG 3'
487 5' CACTGAAATGCGCCTTAATCCTCC 3' — 5' TGATATGGGAGGAGCTGTGAAGGA 3'

488 For each DNA fragment amplified by PCR, both forward and reverse primers were used in the
489 sequencing reactions. The presence of the *mr17* mutation was confirmed in 7 independent sequencing
490 reactions from mutant animals. 2 independent reactions from wildtype animals were used as reference.

491 **Brood size and embryonic lethality assays**

492 To score fertility and embryonic lethality, 10 to 11 individual L4 hermaphrodites grown at 15°C were
493 picked and transferred to individual plates at either 15°C, 20°C or 25°C. Animals were transferred on
494 new plates until they stopped laying eggs, and the number of eggs on individual plates scored each day.
495 After 24h, unhatched eggs and live progeny were scored. Embryonic lethality represents the number of
496 unhatched eggs, divided by the total number of total eggs laid. Experiments were repeated 3 times each.

497 **Visualization of apoptotic cells in the germline**

498 Acridine Orange (Sigma Aldrich #A9231) was used to visualize apoptotic cells in the germline of live
499 animals as previously described (124). Briefly, L4 hermaphrodites grown at permissive temperature
500 (15°C), were placed on NGM plates at the restrictive temperature of 20°C during 18h. 1ml of Acridine
501 Orange diluted at a final concentration of 50µg/ml in M9 buffer was added to the plates and incubated
502 for 2h in the dark. Stained animals were transferred to a fresh NGM plates seeded with OP50 and
503 incubated for 2h in the dark in order to remove stained bacteria in the intestine. Animals were placed on

504 4% agar pad in a drop of 10mM levamisole (Sigma Aldrich #L9756) diluted in M9 buffer, a coverslip
505 was placed on top and sealed with nailed polish. Z-stack images of the posterior gonad were acquired
506 using a Zeiss LSM710 inverted confocal microscope with 40X oil Immersion objective. Z-stack of
507 germlines were acquire every 0.5µm, images correspond to a projection using Max intensity method
508 using Fiji (125). At least 20 gonads were imaged for each genotype.

509

510 **Declarations**

511 **Ethics approval and consent to participate:** not applicable

512 **Consent for publication:** not applicable

513 **Availability of data and materials:** All data generated or analysed during this study are
514 included in this published article [and its supplementary information files]. Gene expression
515 data have been deposited at GEO (awaiting processing)

516 **Competing interests**

517 The authors declare that they have no competing interests

518 **Funding**

519 This work was supported by the ANR (N° 15-CE12-0018-01), the CNRS, and the Fondation ARC

520 **Authors' contributions**

521 FP and MH designed genetic experiments; MH performed and analyzed genetic assays; DL carried out
522 FRAP and FLIM-FRET experiments; AB made genetic constructs and helped with FLIM-FRET
523 acquisition and experimental design; VR helped with experimental design and helped carry out qRT-
524 PCR analysis; MH and LG carried out immunofluorescence analysis; FP and DL wrote the paper; MH,
525 FP and DL prepared figures, and all authors helped with editing; all authors read and approved the final
526 manuscript

527 **Acknowledgements**

528 We thank "Montpellier Ressources Imagerie" (MRI), CGC, which is funded by NIH Office of Research
529 Infrastructure Programs (P40 OD010440) for strains, and the Mitani lab for deletion strains. We

530 gratefully acknowledge support from the PSMN (Pôle Scientifique de Modélisation Numérique) of the
531 ENS de Lyon for computing resources.

532

533

534 **References**

535 1. Rowley MJ, Corces VG. Organizational principles of 3D genome architecture. *Nat Rev Genet.*
536 2018 Dec;19(12):789–800.

537 2. Antonin W, Neumann H. Chromosome condensation and decondensation during mitosis. *Curr*
538 *Opin Cell Biol.* 2016;40:15–22.

539 3. Beck DB, Oda H, Shen SS, Reinberg D. PR-Set7 and H4K20me1: at the crossroads of genome
540 integrity, cell cycle, chromosome condensation, and transcription. *Genes Dev.* 2012 Feb
541 15;26(4):325–37.

542 4. Zhiteneva A, Bonfiglio JJ, Makarov A, Colby T, Vagnarelli P, Schirmer EC, et al. Mitotic post-
543 translational modifications of histones promote chromatin compaction in vitro. *Open Biol.*
544 2017;7(9).

545 5. Hayashi K, Yoshida K, Matsui Y. A histone H3 methyltransferase controls epigenetic events
546 required for meiotic prophase. *Nature.* 2005 Nov;438(7066):374–8.

547 6. Borde V, Robine N, Lin W, Bonfils S, Geli V, Nicolas A. Histone H3 lysine 4 trimethylation
548 marks meiotic recombination initiation sites. *EMBO J.* 2009 Jan 21;28(2):99–111.

549 7. Buard J, Barthès P, Grey C, de Massy B. Distinct histone modifications define initiation and
550 repair of meiotic recombination in the mouse. *EMBO J.* 2009 Sep 2;28(17):2616–24.

551 8. Baudat F, Buard J, Grey C, Fledel-Alon A, Ober C, Przeworski M, et al. PRDM9 is a major
552 determinant of meiotic recombination hotspots in humans and mice. *Science.* 2010 Feb
553 12;327(5967):836–40.

554 9. Eissenberg JC, Shilatfard A. Histone H3 lysine 4 (H3K4) methylation in development and
555 differentiation. *Dev Biol.* 2010 Mar 15;339(2):240–9.

556 10. Dehe PM, Dichtl B, Schaft D, Roguev A, Pamblanco M, Lebrun R, et al. Protein interactions
557 within the Set1 complex and their roles in the regulation of histone 3 lysine 4 methylation. *J Biol*
558 *Chem.* 2006 Nov 17;281(46):35404–12.

559 11. Howe FS, Fischl H, Murray SC, Mellor J. Is H3K4me3 instructive for transcription activation?
560 *BioEssays News Rev Mol Cell Dev Biol.* 2017 Jan;39(1):1–12.

561 12. Vermeulen M, Mulder KW, Denissov S, Pijnappel WW, van Schaik FM, Varier RA, et al.
562 Selective anchoring of TFIID to nucleosomes by trimethylation of histone H3 lysine 4. *Cell.* 2007
563 Oct 5;131(1):58–69.

564 13. Lauberth SM, Nakayama T, Wu X, Ferris AL, Tang Z, Hughes SH, et al. H3K4me3 interactions
565 with TAF3 regulate preinitiation complex assembly and selective gene activation. *Cell.* 2013 Feb
566 28;152(5):1021–36.

- 567 14. Taverna SD, Ilin S, Rogers RS, Tanny JC, Lavender H, Li H, et al. Yng1 PHD finger binding to
568 H3 trimethylated at K4 promotes NuA3 HAT activity at K14 of H3 and transcription at a subset
569 of targeted ORFs. *Mol Cell*. 2006 Dec 8;24(5):785–96.
- 570 15. Yun M, Wu J, Workman JL, Li B. Readers of histone modifications. *Cell Res*. 2011
571 Apr;21(4):564–78.
- 572 16. Lam K-WG, Brick K, Cheng G, Pratto F, Camerini-Otero RD. Cell-type-specific genomics
573 reveals histone modification dynamics in mammalian meiosis. *Nat Commun*. 2019
574 Dec;10(1):3821.
- 575 17. Prakash K, Fournier D, Redl S, Best G, Borsos M, Tiwari VK, et al. Superresolution imaging
576 reveals structurally distinct periodic patterns of chromatin along pachytene chromosomes. *Proc*
577 *Natl Acad Sci U S A*. 2015 Nov 24;112(47):14635–40.
- 578 18. Sha Q-Q, Dai X-X, Jiang J-C, Yu C, Jiang Y, Liu J, et al. CFP1 coordinates histone H3 lysine-4
579 trimethylation and meiotic cell cycle progression in mouse oocytes. *Nat Commun*. 2018
580 28;9(1):3477.
- 581 19. Mikheyeva IV, Grady PJR, Tamburini FB, Lorenz DR, Cam HP. Multifaceted genome control
582 by Set1 Dependent and Independent of H3K4 methylation and the Set1C/COMPASS complex.
583 *PLoS Genet*. 2014 Oct;10(10):e1004740.
- 584 20. Mizuguchi T, Barrowman J, Grewal SIS. Chromosome domain architecture and dynamic
585 organization of the fission yeast genome. *FEBS Lett*. 2015 Oct 7;589(20PartA):2975–86.
- 586 21. Lorenz DR, Mikheyeva IV, Johansen P, Meyer L, Berg A, Grewal SIS, et al. CENP-B cooperates
587 with Set1 in bidirectional transcriptional silencing and genome organization of retrotransposons.
588 *Mol Cell Biol*. 2012 Oct;32(20):4215–25.
- 589 22. Xiao Y, Bedet C, Robert VJ, Simonet T, Dunkelbarger S, Rakotomalala C, et al. *Caenorhabditis*
590 *elegans* chromatin-associated proteins SET-2 and ASH-2 are differentially required for histone
591 H3 Lys 4 methylation in embryos and adult germ cells. *Proc Natl Acad Sci U A*. 2011 May
592 17;108(20):8305–10.
- 593 23. Li T, Kelly WG. A role for Set1/MLL-related components in epigenetic regulation of the
594 *Caenorhabditis elegans* germ line. *PLoS Genet*. 2011 Mar;7(3):e1001349.
- 595 24. Herbertte M, Mercier MG, Michal F, Cluet D, Burny C, Yvert G, et al. The *C. elegans* SET-
596 2/SET1 histone H3 Lys4 (H3K4) methyltransferase preserves genome stability in the germline.
597 *DNA Repair*. 2017 Sep;57:139–50.
- 598 25. Robert VJ, Mercier MG, Bedet C, Janczarski S, Merlet J, Garvis S, et al. The SET-2/SET1 histone
599 H3K4 methyltransferase maintains pluripotency in the *Caenorhabditis elegans* germline. *Cell*
600 *Rep*. 2014 Oct 23;9(2):443–50.
- 601 26. Clouaire T, Webb S, Skene P, Illingworth R, Kerr A, Andrews R, et al. Cfp1 integrates both CpG
602 content and gene activity for accurate H3K4me3 deposition in embryonic stem cells. *Genes Dev*.
603 2012 Aug 1;26(15):1714–28.
- 604 27. Clouaire T, Webb S, Bird A. Cfp1 is required for gene expression-dependent H3K4
605 trimethylation and H3K9 acetylation in embryonic stem cells. *Genome Biol*. 2014 Sep
606 4;15(9):451.
- 607 28. Lenstra TL, Benschop JJ, Kim T, Schulze JM, Brabers NA, Margaritis T, et al. The specificity
608 and topology of chromatin interaction pathways in yeast. *Mol Cell*. 2011 May 20;42(4):536–49.

- 609 29. Weiner A, Chen HV, Liu CL, Rahat A, Klien A, Soares L, et al. Systematic dissection of roles
610 for chromatin regulators in a yeast stress response. *PLoS Biol.* 2012 Jul;10(7):e1001369.
- 611 30. Beurton F, Stempor P, Caron M, Appert A, Dong Y, Chen RA-J, et al. Physical and functional
612 interaction between SET1/COMPASS complex component CFP-1 and a Sin3S HDAC complex
613 in *C. elegans*. *Nucleic Acids Res.* 2019 Dec 2;47(21):11164–80.
- 614 31. Hirano T. Condensins: universal organizers of chromosomes with diverse functions. *Genes Dev.*
615 2012 Aug 1;26(15):1659–78.
- 616 32. Piskadlo E, Oliveira RA. Novel insights into mitotic chromosome condensation. *F1000Research.*
617 2016;5.
- 618 33. Kimble J, Crittenden SL. Germline proliferation and its control. *WormBook Online Rev C*
619 *Elegans Biol.* 2005 Aug 15;1–14.
- 620 34. Fisher K, Southall SM, Wilson JR, Poulin GB. Methylation and demethylation activities of a *C.*
621 *elegans* MLL-like complex attenuate RAS signalling. *Dev Biol.* 2010 May;341(1):142–53.
- 622 35. Engert CG, Droste R, van Oudenaarden A, Horvitz HR. A *Caenorhabditis elegans* protein with a
623 PRDM9-like SET domain localizes to chromatin-associated foci and promotes spermatocyte
624 gene expression, sperm production and fertility. *PLoS Genet.* 2018;14(4):e1007295.
- 625 36. Adriaens C, Serebryanny LA, Feric M, Schibler A, Meaburn KJ, Kubben N, et al. Blank spots
626 on the map: some current questions on nuclear organization and genome architecture. *Histochem*
627 *Cell Biol.* 2018 Dec;150(6):579–92.
- 628 37. Llères D, James J, Swift S, Norman DG, Lamond AI. Quantitative analysis of chromatin
629 compaction in living cells using FLIM–FRET. *J Cell Biol.* 2009 Nov 16;187(4):481–96.
- 630 38. Lou J, Scipioni L, Wright BK, Bartolec TK, Zhang J, Masamsetti VP, et al. Phasor histone FLIM-
631 FRET microscopy quantifies spatiotemporal rearrangement of chromatin architecture during the
632 DNA damage response. *Proc Natl Acad Sci.* 2019 Apr 9;116(15):7323–32.
- 633 39. Sobocki M, Mrouj K, Camasses A, Parisis N, Nicolas E, Llères D, et al. The cell proliferation
634 antigen Ki-67 organises heterochromatin. *eLife.* 2016 Mar 7;5:e13722.
- 635 40. Baarlink C, Plessner M, Sherrard A, Morita K, Misu S, Virant D, et al. A transient pool of nuclear
636 F-actin at mitotic exit controls chromatin organization. *Nat Cell Biol.* 2017 Dec;19(12):1389–
637 99.
- 638 41. Wang Y, Sherrard A, Zhao B, Melak M, Trautwein J, Kleinschnitz E-M, et al. GPCR-induced
639 calcium transients trigger nuclear actin assembly for chromatin dynamics. *Nat Commun.* 2019
640 Dec;10(1):5271.
- 641 42. Llères D, Swift S, Lamond AI. Detecting Protein-Protein Interactions In Vivo with FRET using
642 Multiphoton Fluorescence Lifetime Imaging Microscopy (FLIM). *Curr Protoc Cytom* [Internet].
643 2007 Oct [cited 2020 Feb 28];42(1). Available from:
644 <https://onlinelibrary.wiley.com/doi/abs/10.1002/0471142956.cy1210s42>
- 645 43. Llères D, Bailly AP, Perrin A, Norman DG, Xirodimas DP, Feil R. Quantitative FLIM-FRET
646 Microscopy to Monitor Nanoscale Chromatin Compaction In Vivo Reveals Structural Roles of
647 Condensin Complexes. *Cell Rep.* 2017 Feb 14;18(7):1791–803.
- 648 44. Potapova T, Gorbsky GJ. The Consequences of Chromosome Segregation Errors in Mitosis and
649 Meiosis. *Biology.* 2017 Feb 8;6(1).

- 650 45. Beurton F. Physical and functional interaction between the SET1 complex component CFP-
651 1/CXXC and the Sin-3S/HDAC complex at promoter regions. *Nucleic Acids Res.* 2019 Dec
652 2;47(21):11164–80.
- 653 46. Csankovszki G, Collette K, Spahl K, Carey J, Snyder M, Petty E, et al. Three distinct condensin
654 complexes control *C. elegans* chromosome dynamics. *Curr Biol CB.* 2009 Jan 13;19(1):9–19.
- 655 47. Ono T, Fang Y, Spector DL, Hirano T. Spatial and temporal regulation of Condensins I and II in
656 mitotic chromosome assembly in human cells. *Mol Biol Cell.* 2004 Jul;15(7):3296–308.
- 657 48. Albritton SE, Ercan S. *Caenorhabditis elegans* Dosage Compensation: Insights into Condensin-
658 Mediated Gene Regulation. *Trends Genet TIG.* 2018;34(1):41–53.
- 659 49. Chan RC, Severson AF, Meyer BJ. Condensin restructures chromosomes in preparation for
660 meiotic divisions. *J Cell Biol.* 2004 Nov 22;167(4):613–25.
- 661 50. Mets DG, Meyer BJ. Condensins regulate meiotic DNA break distribution, thus crossover
662 frequency, by controlling chromosome structure. *Cell.* 2009 Oct 2;139(1):73–86.
- 663 51. Gonzalez-Serricchio AS, Sternberg PW. Visualization of *C. elegans* transgenic arrays by GFP.
664 *BMC Genet.* 2006 Jun 7;7:36.
- 665 52. Stear JH, Roth MB. Characterization of HCP-6, a *C. elegans* protein required to prevent
666 chromosome twisting and merotelic attachment. *Genes Dev.* 2002 Jun 15;16(12):1498–508.
- 667 53. Gumienny TL, Lambie E, Hartweg E, Horvitz HR, Hengartner MO. Genetic control of
668 programmed cell death in the *Caenorhabditis elegans* hermaphrodite germline. *Development.*
669 1999 Feb;126(5):1011–22.
- 670 54. Gartner A, Boag PR, Blackwell TK. Germline survival and apoptosis. *WormBook Online Rev C*
671 *Elegans Biol.* 2008 Sep 4;1–20.
- 672 55. Boulton SJ, Martin JS, Polanowska J, Hill DE, Gartner A, Vidal M. BRCA1/BARD1 orthologs
673 required for DNA repair in *Caenorhabditis elegans*. *Curr Biol.* 2004 Jan 6;14(1):33–9.
- 674 56. O’Connell KF, Leys CM, White JG. A genetic screen for temperature-sensitive cell-division
675 mutants of *Caenorhabditis elegans*. *Genetics.* 1998 Jul;149(3):1303–21.
- 676 57. Adachi Y, Luke M, Laemmli UK. Chromosome assembly in vitro: topoisomerase II is required
677 for condensation. *Cell.* 1991 Jan 11;64(1):137–48.
- 678 58. Hirano T, Mitchison TJ. Topoisomerase II does not play a scaffolding role in the organization of
679 mitotic chromosomes assembled in *Xenopus* egg extracts. *J Cell Biol.* 1993 Feb;120(3):601–12.
- 680 59. Uemura T, Ohkura H, Adachi Y, Morino K, Shiozaki K, Yanagida M. DNA topoisomerase II is
681 required for condensation and separation of mitotic chromosomes in *S. pombe*. *Cell.* 1987
682 Sep;50(6):917–25.
- 683 60. Ladouceur A-M, Ranjan R, Smith L, Fadero T, Heppert J, Goldstein B, et al. CENP-A and
684 topoisomerase-II antagonistically affect chromosome length. *J Cell Biol.* 2017 04;216(9):2645–
685 55.
- 686 61. Marchetti F, Bishop JB, Lowe X, Generoso WM, Hozier J, Wyrobek AJ. Etoposide induces
687 heritable chromosomal aberrations and aneuploidy during male meiosis in the mouse. *Proc Natl*
688 *Acad Sci.* 2001 Mar 27;98(7):3952–7.

- 689 62. Li X-M, Yu C, Wang Z-W, Zhang Y-L, Liu X-M, Zhou D, et al. DNA Topoisomerase II Is
690 Dispensable for Oocyte Meiotic Resumption but Is Essential for Meiotic Chromosome
691 Condensation and Separation in Mice1. *Biol Reprod* [Internet]. 2013 Nov 1 [cited 2019 Aug
692 22];89(5). Available from: [https://academic.oup.com/biolreprod/article-](https://academic.oup.com/biolreprod/article-lookup/doi/10.1095/biolreprod.113.110692)
693 [lookup/doi/10.1095/biolreprod.113.110692](https://academic.oup.com/biolreprod/article-lookup/doi/10.1095/biolreprod.113.110692)
- 694 63. Gómez R, Viera A, Berenguer I, Llano E, Pendás AM, Barbero JL, et al. Cohesin removal
695 precedes topoisomerase II α -dependent decatenation at centromeres in male mammalian meiosis
696 II. *Chromosoma*. 2014 Mar;123(1–2):129–46.
- 697 64. Hughes SE, Hawley RS. Topoisomerase II is required for the proper separation of
698 heterochromatic regions during *Drosophila melanogaster* female meiosis. *PLoS Genet*. 2014
699 Oct;10(10):e1004650.
- 700 65. Jaramillo-Lambert A, Fabritius AS, Hansen TJ, Smith HE, Golden A. The Identification of a
701 Novel Mutant Allele of topoisomerase II in *Caenorhabditis elegans* Reveals a Unique Role in
702 Chromosome Segregation During Spermatogenesis. *Genetics*. 2016 Dec;204(4):1407–22.
- 703 66. Rog O, Dernburg AF. Chromosome pairing and synapsis during *Caenorhabditis elegans* meiosis.
704 *Curr Opin Cell Biol*. 2013 Jun;25(3):349–56.
- 705 67. Liang Z, Zickler D, Prentiss M, Chang FS, Witz G, Maeshima K, et al. Chromosomes Progress
706 to Metaphase in Multiple Discrete Steps via Global Compaction/Expansion Cycles. *Cell*. 2015
707 May 21;161(5):1124–37.
- 708 68. Nagasaka K, Hossain MJ, Roberti MJ, Ellenberg J, Hirota T. Sister chromatid resolution is an
709 intrinsic part of chromosome organization in prophase. *Nat Cell Biol*. 2016;18(6):692–9.
- 710 69. Oliveira RA, Hamilton RS, Pauli A, Davis I, Nasmyth K. Cohesin cleavage and Cdk inhibition
711 trigger formation of daughter nuclei. *Nat Cell Biol*. 2010 Feb;12(2):185–92.
- 712 70. DiNardo S, Voelkel K, Sternglanz R. DNA topoisomerase II mutant of *Saccharomyces*
713 *cerevisiae*: topoisomerase II is required for segregation of daughter molecules at the termination
714 of DNA replication. *Proc Natl Acad Sci*. 1984 May 1;81(9):2616–20.
- 715 71. Sundin O, Varshavsky A. Terminal stages of SV40 DNA replication proceed via multiply
716 intertwined catenated dimers. *Cell*. 1980 Aug;21(1):103–14.
- 717 72. Chen RA-J, Stempor P, Down TA, Zeiser E, Feuer SK, Ahringer J. Extreme HOT regions are
718 CpG-dense promoters in *C. elegans* and humans. *Genome Res*. 2014 Jul;24(7):1138–46.
- 719 73. Simonet T, Dulermo R, Schott S, Palladino F. Antagonistic functions of SET-2/SET1 and
720 HPL/HP1 proteins in *C. elegans* development. *Dev Biol*. 2007 Dec 1;312(1):367–83.
- 721 74. Christensen J, Agger K, Cloos PA, Pasini D, Rose S, Sennels L, et al. RBP2 belongs to a family
722 of demethylases, specific for tri- and dimethylated lysine 4 on histone 3. *Cell*. 2007 Mar
723 23;128(6):1063–76.
- 724 75. Alvares SM, Mayberry GA, Joyner EY, Lakowski B, Ahmed S. H3K4 demethylase activities
725 repress proliferative and postmitotic aging. *Aging Cell*. 2014 Apr;13(2):245–53.
- 726 76. Lussi YC, Mariani L, Friis C, Peltonen J, Myers TR, Krag C, et al. Impaired removal of H3K4
727 methylation affects cell fate determination and gene transcription. *Dev Camb Engl*. 2016
728 15;143(20):3751–62.

- 729 77. Greer EL, Maures TJ, Hauswirth AG, Green EM, Leeman DS, Maro GS, et al. Members of the
730 H3K4 trimethylation complex regulate lifespan in a germline-dependent manner in *C. elegans*.
731 *Nature*. 2010 Jul;466(7304):383–7.
- 732 78. Wang J, Barr MM. RNA Interference in *Caenorhabditis elegans*. In: *Methods in Enzymology*
733 [Internet]. Elsevier; 2005 [cited 2020 Feb 11]. p. 36–55. Available from:
734 <https://linkinghub.elsevier.com/retrieve/pii/S0076687904920034>
- 735 79. Ganji M, Shaltiel IA, Bisht S, Kim E, Kalichava A, Haering CH, et al. Real-time imaging of
736 DNA loop extrusion by condensin. *Science*. 2018 06;360(6384):102–5.
- 737 80. Gibcus JH, Samejima K, Goloborodko A, Samejima I, Naumova N, Nuebler J, et al. A pathway
738 for mitotic chromosome formation. *Science*. 2018 09;359(6376).
- 739 81. Samejima K, Samejima I, Vagnarelli P, Ogawa H, Vargiu G, Kelly DA, et al. Mitotic
740 chromosomes are compacted laterally by KIF4 and condensin and axially by topoisomerase II α .
741 *J Cell Biol*. 2012 Nov 26;199(5):755–70.
- 742 82. Wilkins BJ, Rall NA, Ostwal Y, Kruitwagen T, Hiragami-Hamada K, Winkler M, et al. A
743 Cascade of Histone Modifications Induces Chromatin Condensation in Mitosis. *Science*. 2014
744 Jan 3;343(6166):77–80.
- 745 83. Georgatos SD, Markaki Y, Christogianni A, Politou AS. Chromatin remodeling during mitosis:
746 a structure-based code? *Front Biosci Landmark Ed*. 2009 Jan 1;14:2017–27.
- 747 84. Kruitwagen T, Denoth-Lippuner A, Wilkins BJ, Neumann H, Barral Y. Axial contraction and
748 short-range compaction of chromatin synergistically promote mitotic chromosome condensation.
749 *eLife*. 2015 Nov 28;4:e1039.
- 750 85. Markaki Y, Christogianni A, Politou AS, Georgatos SD. Phosphorylation of histone H3 at Thr3
751 is part of a combinatorial pattern that marks and configures mitotic chromatin. *J Cell Sci*. 2009
752 Aug 15;122(Pt 16):2809–19.
- 753 86. Batty P, Gerlich DW. Mitotic Chromosome Mechanics: How Cells Segregate Their Genome.
754 *Trends Cell Biol*. 2019 Sep;29(9):717–26.
- 755 87. Vagnarelli P, Hudson DF, Ribeiro SA, Trinkle-Mulcahy L, Spence JM, Lai F, et al. Condensin
756 and Repo-Man-PP1 co-operate in the regulation of chromosome architecture during mitosis. *Nat*
757 *Cell Biol*. 2006 Oct;8(10):1133–42.
- 758 88. Hudson DF, Vagnarelli P, Gassmann R, Earnshaw WC. Condensin Is Required for Nonhistone
759 Protein Assembly and Structural Integrity of Vertebrate Mitotic Chromosomes. *Dev Cell*. 2003
760 Aug;5(2):323–36.
- 761 89. Ono T, Losada A, Hirano M, Myers MP, Neuwald AF, Hirano T. Differential contributions of
762 condensin I and condensin II to mitotic chromosome architecture in vertebrate cells. *Cell*. 2003
763 Oct 3;115(1):109–21.
- 764 90. Samoshkin A, Arnautov A, Jansen LET, Ouspenski I, Dye L, Karpova T, et al. Human
765 condensin function is essential for centromeric chromatin assembly and proper sister kinetochore
766 orientation. *PloS One*. 2009 Aug 28;4(8):e6831.
- 767 91. Yoshimura SH, Hirano T. HEAT repeats - versatile arrays of amphiphilic helices working in
768 crowded environments? *J Cell Sci*. 2016 01;129(21):3963–70.

- 769 92. Hernandez MR, Davis MB, Jiang J, Brouhard EA, Severson AF, Csankovszki G. Condensin I
770 protects meiotic cohesin from WAPL-1 mediated removal. *PLoS Genet.* 2018;14(5):e1007382.
- 771 93. Hong Y, Sonnevile R, Agostinho A, Meier B, Wang B, Blow JJ, et al. The SMC-5/6 Complex
772 and the HIM-6 (BLM) Helicase Synergistically Promote Meiotic Recombination Intermediate
773 Processing and Chromosome Maturation during *Caenorhabditis elegans* Meiosis. *PLoS Genet.*
774 2016 Mar;12(3):e1005872.
- 775 94. Belmont AS. Mitotic chromosome scaffold structure: New approaches to an old controversy.
776 *Proc Natl Acad Sci.* 2002 Dec 10;99(25):15855–7.
- 777 95. Gasser SM, Laroche T, Falquet J, Boy de la Tour E, Laemmli UK. Metaphase chromosome
778 structure. *J Mol Biol.* 1986 Apr;188(4):613–29.
- 779 96. Anderson H, Roberge M. Topoisomerase II inhibitors affect entry into mitosis and chromosome
780 condensation in BHK cells. *Cell Growth Differ Mol Biol J Am Assoc Cancer Res.* 1996
781 Jan;7(1):83–90.
- 782 97. Cuvier O, Hirano T. A role of topoisomerase II in linking DNA replication to chromosome
783 condensation. *J Cell Biol.* 2003 Mar 3;160(5):645–55.
- 784 98. Gonzalez RE, Lim C-U, Cole K, Bianchini CH, Schools GP, Davis BE, et al. Effects of
785 conditional depletion of topoisomerase II on cell cycle progression in mammalian cells. *Cell*
786 *Cycle Georget Tex.* 2011 Oct 15;10(20):3505–14.
- 787 99. Petrova B, Dehler S, Kruitwagen T, Hériché J-K, Miura K, Haering CH. Quantitative analysis of
788 chromosome condensation in fission yeast. *Mol Cell Biol.* 2013 Mar;33(5):984–98.
- 789 100. Sakaguchi A, Kikuchi A. Functional compatibility between isoform alpha and beta of type II
790 DNA topoisomerase. *J Cell Sci.* 2004 Mar 1;117(Pt 7):1047–54.
- 791 101. Shintomi K, Takahashi TS, Hirano T. Reconstitution of mitotic chromatids with a minimum set
792 of purified factors. *Nat Cell Biol.* 2015 Aug;17(8):1014–23.
- 793 102. Buchenau P, Saumweber H, Arndt-Jovin DJ. Consequences of topoisomerase II inhibition in
794 early embryogenesis of *Drosophila* revealed by in vivo confocal laser scanning microscopy. *J*
795 *Cell Sci.* 1993 Apr;104 (Pt 4):1175–85.
- 796 103. Vas ACJ, Andrews CA, Kirkland Matesky K, Clarke DJ. In Vivo Analysis of Chromosome
797 Condensation in *Saccharomyces cerevisiae*. Bloom K, editor. *Mol Biol Cell.* 2007
798 Feb;18(2):557–68.
- 799 104. Klein F. Localization of RAP1 and topoisomerase II in nuclei and meiotic chromosomes of yeast.
800 *J Cell Biol.* 1992 Jun 1;117(5):935–48.
- 801 105. Yu C, Fan X, Sha Q-Q, Wang H-H, Li B-T, Dai X-X, et al. CFP1 Regulates Histone H3K4
802 Trimethylation and Developmental Potential in Mouse Oocytes. *Cell Rep.* 2017
803 Aug;20(5):1161–72.
- 804 106. Blat Y, Protacio RU, Hunter N, Kleckner N. Physical and functional interactions among basic
805 chromosome organizational features govern early steps of meiotic chiasma formation. *Cell.* 2002
806 Dec 13;111(6):791–802.
- 807 107. McNicoll F, Stevense M, Jessberger R. Cohesin in Gametogenesis. In: *Current Topics in*
808 *Developmental Biology* [Internet]. Elsevier; 2013 [cited 2019 Oct 9]. p. 1–34. Available from:
809 <https://linkinghub.elsevier.com/retrieve/pii/B9780124160248000015>

- 810 108. Panizza S, Mendoza MA, Berlinger M, Huang L, Nicolas A, Shirahige K, et al. Spo11-accessory
811 proteins link double-strand break sites to the chromosome axis in early meiotic recombination.
812 *Cell*. 2011 Aug 5;146(3):372–83.
- 813 109. West AM, Rosenberg SC, Ur SN, Lehmer MK, Ye Q, Hagemann G, et al. A conserved
814 filamentous assembly underlies the structure of the meiotic chromosome axis. *eLife*. 2019 Jan
815 18;8.
- 816 110. Patel L, Kang R, Rosenberg SC, Qiu Y, Raviram R, Chee S, et al. Dynamic reorganization of the
817 genome shapes the recombination landscape in meiotic prophase. *Nat Struct Mol Biol*. 2019
818 Mar;26(3):164–74.
- 819 111. Yuen KC, Slaughter BD, Gerton JL. Condensin II is anchored by TFIIC and H3K4me3 in the
820 mammalian genome and supports the expression of active dense gene clusters. *Sci Adv*.
821 2017;3(6):e1700191.
- 822 112. Kim H, Yen L, Wongpalee SP, Kirshner JA, Mehta N, Xue Y, et al. The Gene-Silencing Protein
823 MORC-1 Topologically Entraps DNA and Forms Multimeric Assemblies to Cause DNA
824 Compaction. *Mol Cell*. 2019 22;75(4):700-710.e6.
- 825 113. Weiser NE, Yang DX, Feng S, Kalinava N, Brown KC, Khanikar J, et al. MORC-1 Integrates
826 Nuclear RNAi and Transgenerational Chromatin Architecture to Promote Germline Immortality.
827 *Dev Cell*. 2017 22;41(4):408-423.e7.
- 828 114. Alavattam KG, Maezawa S, Sakashita A, Khoury H, Barski A, Kaplan N, et al. Attenuated
829 chromatin compartmentalization in meiosis and its maturation in sperm development. *Nat Struct
830 Mol Biol*. 2019;26(3):175–84.
- 831 115. Jabbari K, Wirtz J, Rauscher M, Wiehe T. A common genomic code for chromatin architecture
832 and recombination landscape. *PloS One*. 2019;14(3):e0213278.
- 833 116. Schalbetter SA, Fudenberg G, Baxter J, Pollard KS, Neale MJ. Principles of meiotic chromosome
834 assembly revealed in *S. cerevisiae*. *Nat Commun*. 2019 22;10(1):4795.
- 835 117. Wang Y, Wang H, Zhang Y, Du Z, Si W, Fan S, et al. Reprogramming of Meiotic Chromatin
836 Architecture during Spermatogenesis. *Mol Cell*. 2019 Feb;73(3):547-561.e6.
- 837 118. MacGregor IA, Adams IR, Gilbert N. Large-scale chromatin organisation in interphase, mitosis
838 and meiosis. *Biochem J*. 2019 Aug 15;476(15):2141–56.
- 839 119. Naumova N, Imakaev M, Fudenberg G, Zhan Y, Lajoie BR, Mirny LA, et al. Organization of the
840 mitotic chromosome. *Science*. 2013 Nov 22;342(6161):948–53.
- 841 120. Brenner S. The Genetics of *Caenorhabditis elegans*. *Genetics*. 1974;77(1):71–94.
- 842 121. T., Förster. Experimental and theoretical investigation of the intermolecular transfer of electronic
843 excitation energy. *Z Naturforsch A*. 1949;4:321–7.
- 844 122. Kadyk LC, Kimble J. Genetic regulation of entry into meiosis in *Caenorhabditis elegans*. *Dev
845 Camb Engl*. 1998 May;125(10):1803–13.
- 846 123. Heestand B, Simon M, Frenk S, Titov D, Ahmed S. Transgenerational Sterility of Piwi Mutants
847 Represents a Dynamic Form of Adult Reproductive Diapause. *Cell Rep*. 2018 03;23(1):156–71.

- 848 124. Papaluca A, Ramotar D. A novel approach using *C. elegans* DNA damage-induced apoptosis to
849 characterize the dynamics of uptake transporters for therapeutic drug discoveries. *Sci Rep.* 2016
850 27;6:36026.
- 851 125. Schindelin J, Arganda-Carreras I, Frise E, Kaynig V, Longair M, Pietzsch T, et al. Fiji: an open-
852 source platform for biological-image analysis. *Nat Methods.* 2012 Jun 28;9(7):676–82.
- 853 126. Afgan E, Baker D, Batut B, van den Beek M, Bouvier D, Cech M, et al. The Galaxy platform for
854 accessible, reproducible and collaborative biomedical analyses: 2018 update. *Nucleic Acids Res.*
855 2018 02;46(W1):W537–44.
- 856 127. Love MI, Huber W, Anders S. Moderated estimation of fold change and dispersion for RNA-
857 seq data with DESeq2. *Genome Biol.* 2014;15(12):550.
- 858 128. Zhuang JJ, Banse SA, Hunter CP. The nuclear argonaute NRDE-3 contributes to transitive RNAi
859 in *Caenorhabditis elegans*. *Genetics.* 2013 May;194(1):117–31.

860

861 **Figure 1. *set-2* inactivation influences nanoscale chromatin compaction in the germline. (A)**

862 Fluorescence intensities of GFP-H2B (green) and mCherry-H2B (red) from pachytene-stage germ cells
863 expressing H2B-2FPs. FLIM (right) images of H2B-2FPs pachytene-stage cells. The spatial distribution
864 of the mean fluorescence lifetime (τ) at each pixel is shown for wildtype (*wt* H2B-2FPs cells) (top) or *set-*
865 *2(bn129)* H2B-2FPs mutant animals (bottom). Fluorescence lifetime values ranging between 2.2-3 ns are
866 represented using a continuous pseudo-color scale. Scale bars, 10 μ m. **(B)** Statistical analysis of the
867 FRET efficiency relative to control (*wt*), presented as box-and-whisker plots. The mean FRET value is
868 indicated by a cross in each box. **** $p < 0.0001$ (two-tailed unpaired t test). **(C)** Relative fraction of
869 FRET populations (sub-low, low, intermediate, and high) as defined previously (43) from *wt* and *set-*
870 *2(bn129)* pachytene nuclei. * $p < 0.05$; (two-tailed unpaired t test); n.s, non-significant. n=5 gonads
871 (approx. 350 nuclei) for *wt*, n=6 gonads (approx. 430 nuclei) for *set-2(bn129)*.

872

873 **Figure 2. *set-2* inactivation enhances condensin-II depletion phenotypes. (A) *C. elegans* condensin**

874 subunits and their vertebrate homologs. **(B)** Confocal images of distal germline region from wildtype
875 and *set-2(bn129)* animals treated with empty vector or *kle-2* RNAi. Representative images show
876 examples of "wildtype-like" and "strong" phenotypes, with their presence indicated as percentage (%)
877 of total (n=900, from 9 independent biological replicates) (scale bar, 20 μ m). Arrow indicates the
878 presence of chromatin bridge (scale bar, 10 μ m). Images correspond to a Max intensity projection using

879 Fiji. (C) *kle-2* and *capg-1* mRNA levels in wildtype and *set-2(bn129)* mutant animals after RNAi
880 directed against the respective genes. Relative fold change was calculated with respect to empty vector
881 condition, following normalization with *pmp-3* and *cdc-42*. [*] $p < 0.05$ t-test. (D) Percentage of
882 germlines with "strong" phenotype after RNAi directed against condensin-II (*smc-4*, *capg-2*, *kle-2* and
883 *hcp-6*), condensins-I (*capg-1*, *dpy-28*) and condensin-Idc (*dpy-27*) in wildtype or *set-2(bn129)* mutants.
884 n= number of animals scored from 9 independent experiments for *smc-4* and *kle-2*, 4 for *hcp-6*, and 5
885 for *capg-1* and *capg-2*, and 2 for *dpy-28* and *dpy-27*. All scoring was performed in blind. [***] $p < 0.001$
886 (t-test).

887

888 **Figure 3. Enhancement of *hcp-6(mr17)* phenotypes in *set-2(bn129)* mutant animals.** (A) Schematic
889 diagram of HCP-6 protein and position of the *mr17* mutation. Conserved ARM/HEAT and Cnd1
890 (Condensin complex subunit 1) domains are highlighted in red. (B) Brood size per animals at indicated
891 temperatures (15°C, 20°, 25°C), (n=11 animals per genotypes at 15°C and 25°C, and 33 at 20°C). [***]
892 $p < 0.001$, [*] < 0.05 (t-test adjusted for multiple comparison with the Bonferroni method). (C)
893 Representative confocal images of germlines stained by orange acridine. Asterisks indicate apoptotic
894 cells. (D) quantification of the number of apoptotic cells in the germline of animals switched at 20°C
895 for 24h (n>20 gonads per genotypes). A Wilcoxon test was performed after a significant differences with
896 a Kruskal Wallis test, [ns] non significant difference, [*] $p < 0.05$, [***] $p < 0.001$, [****] $p < 0.0001$.

897

898 **Figure 4. Enhancement of the *top-2* mutant phenotype in absence of *set-2*.** (A) Representative
899 images of DAPI stained adult germlines showing different phenotypic classes. (Scale bar, 10 μm). (B)
900 Scoring of phenotypic classes. Animals were shifted to 24°C at the L1 stage and allowed to develop to
901 adulthood. Germlines categories are as defined in Materials and Methods. **** $p < 0.0001$, *** $p < 0.001$
902 significant difference between mutant backgrounds using chi-square test and FDR correction (ns: non-
903 significant). Scale bar, 50 μm . (C) Enlargement of pachytene and diakinetik nuclei from wildtype or
904 mutant animals. For *top-2* single and *top-2;set-2* double mutants, representative nuclei from normal
905 (left) and short (right) germlines are shown. Nuclei containing more than 6 DAPI stained bodies were

906 observed in both "short" and "normal" germlines. **(D)** Scoring of aneuploid nuclei from cells in
907 diakinesis (Scale bar, 10 μ m).

908

909 **Figure 5. Inactivation of COMPASS targeting component *cfp-1* mimics *set-2* inactivation. (A)**

910 Percentage of germlines with "strong" phenotype after RNAi directed against condensin-II (*smc-4* or
911 *kle-2*) in wildtype, *cfp-1(tm6369)* and *rbr-2(tm1231)* mutants. n= number of animals scored from at
912 least 3 independent experiments. $p < 0.05$, [***] $p < 0.001$, [****] $p < 0.0001$ (t-test); ns, not significant.

913 **(B)** Decreased chromatin compaction in *cfp-1* mutant germlines. Spatial distribution of the mean
914 fluorescence lifetime is shown for wildtype (wt $H2B-2FPs$) or *cfp-1 H2B-2FPs* mutant animals. Fluorescence
915 lifetime values (τ) ranging from 2.0 ns to 2.8 ns are represented using a continuous pseudo-color scale.

916 Scale bars, 10 μ m. Statistical analysis of the FRET efficiency relative to control wt is presented as box-
917 and-whisker plots. Mean FRET value is indicated by a cross in each box. * $p < 0.05$ (two-tailed unpaired
918 t test). n=13 gonads for wt, n=11 gonads for *cfp-1*.

919

920 **Figure 6. Working model for cooperation between COMPASS, condensin-II and TOP-2 in**

921 **chromosome organization.** In wild type, proper chromosome compaction results from the activity of
922 condensin-I (connected yellow circles), condensin-II (connected orange circles) and TOP-2 (blue broken
923 ring). The concerted action of condensins results in the formation of arrays of helical loops, with
924 condensin-II generating outer loops and condensin-I forming inner loops (80). TOP-2 may contribute to
925 compaction by modulating chromatin loops (60), or actively introducing self-entanglement in DNA
926 (32). COMPASS may mediate interactions between loops, possibly by contributing to the clustering of
927 transcribed loci (110). The absence of COMPASS results in subtle defects in chromosome organization
928 (weakly disorganized chromatin), but overall chromosome architecture is maintained by the action of
929 condensins, TOP-2 and additional proteins. Partial depletion of condensin-II or TOP-2 in the absence of
930 COMPASS results in cumulative defects in chromosome organization.

931

932 **Supplementary data**

933 **H3K4me3 Immunostaining**

934 Immunostaining was as previously described (25). Z-stack images of gonads were acquired using a Zeiss
935 LSM710 inverted confocal microscope with 40X oil Immersion objective. Z-stack of germlines were
936 acquired every 0.25 μ m, images correspond to a projection using Max intensity method and Fiji macros.
937 Antisera and the dilutions used were as followed: rabbit anti H3K4me3 (Diagenode, 15310003[CS-
938 003100]; 1:12000) and anti-rabbit Alexa Fluor 555 (Invitrogen/Molecular probes #A21428; 1:1000).

939 **Scoring condensin I RNAi animals**

940 For scoring the efficacy of RNAi, wildtype or *set-2(bn129)* L4 stage animals were transferred to the
941 same RNAi plates used for scoring germline phenotypes and allowed to develop into adults at 20°C.
942 Following 24hrs of egg laying, animals were removed and the body length of F1 progeny measured 3
943 days later, at the L4 stage (based on vulval morphology). Animals were placed on 4% agar pads in 1X
944 M9 complemented with 10mM Levamisole, and observed by DIC on an Axio Imager A2 microscope
945 and EC plan Neofluar 10X/0.5 objective. Length of individual worms was measured using Fiji macros.

946 **Scoring embryonic viability**

947 Between 10 to 20 L4 hermaphrodites grown at the permissive temperature (15°C), were placed on NGM
948 plates at the restrictive temperature of 20°C during 24h, then removed. Eggs laid were allowed to
949 develop during 24h at 20°C (Normal development takes 18h at 20°C from fertilization to hatching).
950 Then dead eggs and larvae were recovered in 1X M9 and washed twice in 1X M9 in order to remove
951 bacteria. Eggs and larvae were placed on 4% agar pads and a coverslip was placed on top. The stage of
952 embryos was determined by DIC observation with EC Plan-Neofluar 100X/1.3 oil objective and
953 AxioImager A2 (Zeiss). At least 75 embryos were scored per genotypes, and the experiment repeated 3
954 independent times.

955 **RNA sequencing of dissected gonads**

956 Gonad dissections and extractions were performed as in (25). Briefly, prior to dissection worms were
957 placed on NGM plates without food to expel bacteria from the gut. Gonads of 5 to 7 young adults at the

958 L4 stage + 12 h were dissected in dissection buffer (Egg Buffer 1.1 X (HEPES pH 7.3 25 mM, NaCl
959 118 mM, KCL 48 mM, CaCl₂ 2 mM, 2 mM MgCl₂), 0.5 mM Levamisole, 0.1% Tween 20) on slides.
960 Extruded gonads were cut at the elbow and the distal part recovered using a drawn capillary and
961 transferred to 30 µl of XB extraction buffer (Kit Picopure, Life technology, # 12204-01), frozen in liquid
962 nitrogen and stored at -80 ° C. For RNA preparation tubes were thawed, the volume of XB extraction
963 buffer adjusted to 100 µl, and RNA purified using the PicoPure kit (Life Technology, # 12204-01)
964 according to the manufacturer's instructions. Elution was in 13 µl of nuclease-free water. The integrity
965 of RNA was evaluated using Tape Station 4200 (Agilent), and the concentration of RNA measured using
966 DropSense 96 (Trinean). Construction of rRNA depleted libraries was carried out at the GenomEast
967 platform (IGBMC, Strasbourg, France), and sequencing by an Illumina HiSeq 4000 device.
968 Bioinformatic analysis was carried out under Galaxy (126). Sequence reads were mapped onto the
969 reference genome (WS254) with the RNA-STAR tool (Version 2.4.1d). Sequences with a quality of
970 cartography lower than 10 were removed with SAMtools (Version 0.1.19). The expression level of each
971 gene for each sample was calculated with htseq-count (Version 0.7.2). Differential analysis of gene
972 expression between the different strains was carried out with the DESeq2 package version 1.16.1 (127)
973 under R version 3.4.4. Additional analyzes were performed with R.

974

975 **Table S1. Genes misregulated in dissected gonads from *set-2* mutant animals**

976

977 **Figure S1. *set-2* inactivation differentially impacts H3K4me3 in the germline** (A) Z-projection of
978 confocal images through the mitotic region, early-mid pachytene and late pachytene nuclei, and
979 diakinesis. Gonads were dissected, fixed and probed with rabbit anti-H3K4me3 antibodies (Diagenode,
980 #15310003) and counter-stained with DAPI. Images were taken with the same laser parameter for each
981 condition. (Scale bar, 10 µm). (B) Confocal images of DAPI stained germlines of fertile wildtype
982 animals and sterile *set-2(bn129)* after 4 generations at 25°C. (Scale bar, 10 µm).

983

984 **Figure S2. Tagged histones H2B are correctly expressed and incorporated into chromatin in *set-2***
985 **mutants.** (A) Mean fluorescence intensity of fluorescently-tagged H2B histones (GFP-H2B and

986 mCherry-H2B) from wt and *set-2(bn129)* mutant pachytene cells. Each data point shows the mean
987 fluorescence intensity \pm S.D. from 8 and 12 gonads representing 549 and 698 nuclei from wt and *set-*
988 *2(bn129)*, respectively. **(B)** Normalized fluorescence intensity recovery of GFP-H2B from wt (black
989 squares) and *set-2(bn129)* (red squares) pachytene cells after laser photo-bleaching (FRAP
990 experiments). Each data point shows the mean \pm S.D. for 11 and 8 pachytene cells from wt and *set-*
991 *2(bn129)*, respectively.

992

993 **Figure S3. Polyploid cells resulting from *kle-2* knockdown in *set-2* mutant germlines.** Wildtype
994 diploid cells carrying a GFP LacO cassette integrated on chromosome IV and expressing lacI show 2
995 GFP spots/nucleus. Polyploid nuclei from *kle-2(RNAi);set-2* germlines showing a strong phenotype are
996 larger and show more than two GFP spots (circled in white) (Scale bar, 10 μ m).

997

998 **Figure S4. Condensin I depletion in wildtype and *set-2* mutant animals results in similar reduction**
999 **in body size.** Condensin I knock down animals are smaller in length than control empty vector (*dpy*
1000 phenotype (128). A similar decrease in body size was observed in wildtype and *set-2* mutants. [****] p
1001 <0.0001 (t-test). ns, not significant. For wild type: empty vector n=32, *capg-1* RNAi n=23, *dpy-27* RNAi
1002 n=29, *dpy-28* RNAi n=30; for *set-2(bn129)*: empty vector n=31, *capg-1* RNAi n=26, *dpy-27* RNAi
1003 n=30, *dpy-28* RNAi n=26

1004

1005 **Figure S5. Germline defects of *hcp-6(mr17)* mutant animals and suppression of *hcp-6(mr17)***
1006 **embryonic lethality.** **(A)** *hcp-6(mr17)* gonads are highly disorganized. Young adult wildtype, *set-2*, *hcp-*
1007 *6* and *set-2;hcp-6* mutant animals shifted to 25°C at the L4 stage were DAPI stained and observed on
1008 AxioImager A2 (Zeiss). **(B)** *set-2* partially suppresses the embryonic lethality of *hcp-6(mr17)* mutants.
1009 Percentage of embryonic lethality at 20°C. [*] p < 0.05 (t-test). number of progeny scored for wildtype,
1010 *set-2(bn129)*, *hcp-6(mr17)* and *hcp-6(mr17);set-2(bn129)* mutants was 10109, 8227, 8757 and 3961,
1011 respectively. 3 independent biological replicates were performed for each genotype.

1012

1013 **Figure S6. Loss of H3K4me3 in *cfp-1* mutant germline and efficacy and scoring of *cfp-1* and *rbr-2***
1014 **RNAi in independent experiments. (A)** decreased H3K4me3 in *cfp-1(tm6369)* mutant germline. **(B)**
1015 *kle-2* mRNA levels in wt, *cfp-1(tm6369)* and *rbr-2(tm1231)* mutant animals. For each of the three
1016 independent experiments, relative fold change was calculated with respect to empty vector condition,
1017 following normalization with *pmp-3* and *cdc-42*. **(C)** Percentage of germlines with "strong" phenotype
1018 in each of the three replicas after RNAi directed against *kle-2* RNAi. Note that although the efficacy of
1019 *kle-2* mRNA knockdown varied between the three experiments, the % of abnormal germlines scored
1020 for each genotype (wt, *cfp-1* and *rbr-2*) was highly similar.

Figures

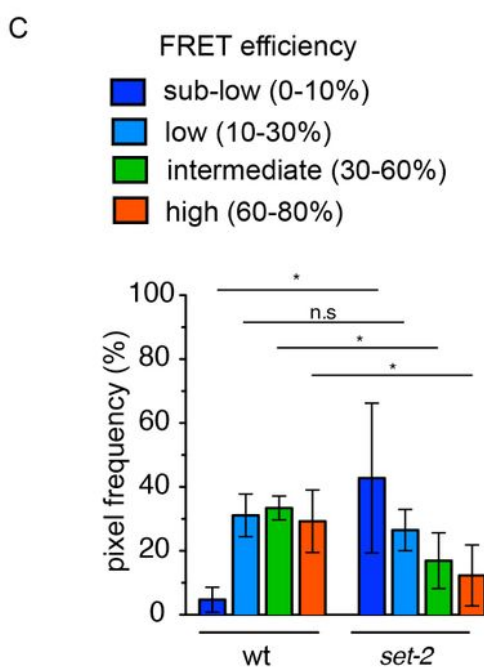
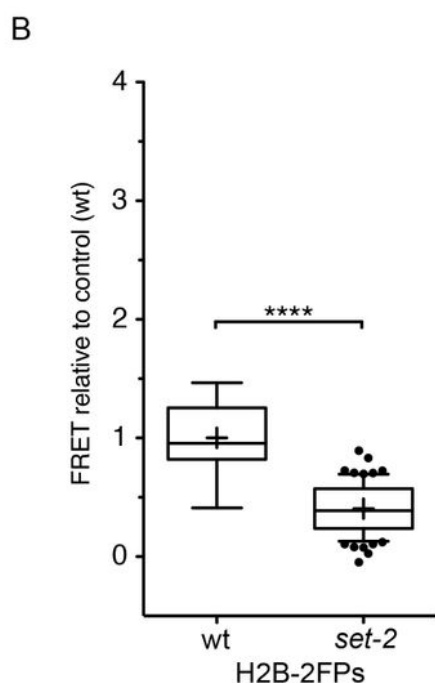
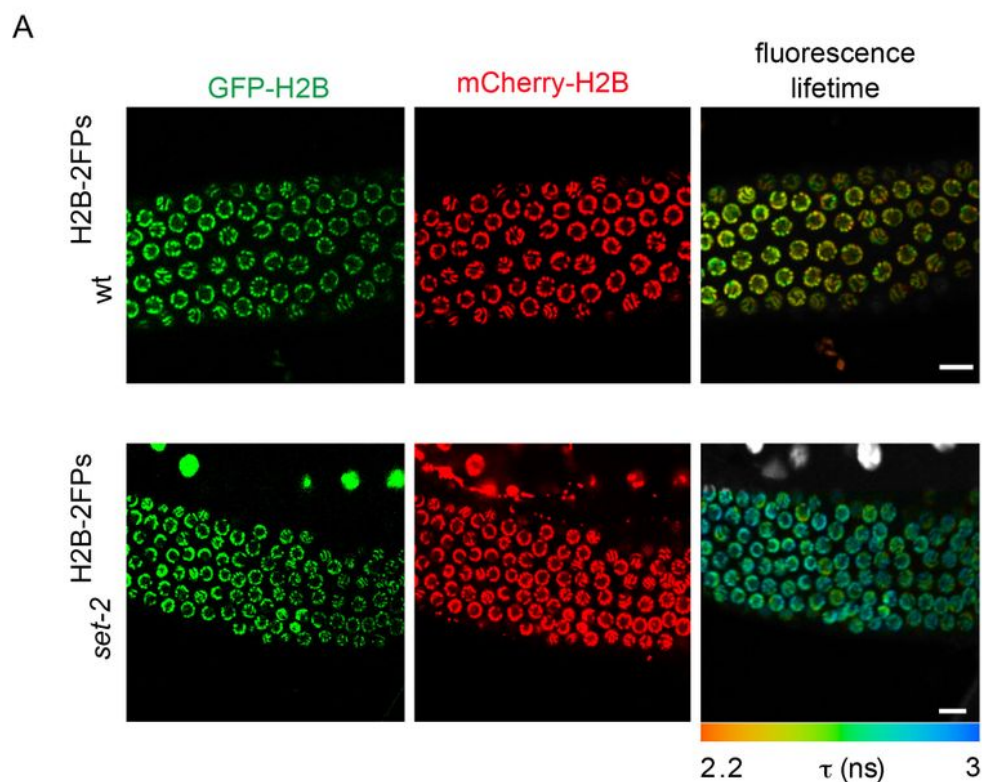


Figure 1

set-2 inactivation influences nanoscale chromatin compaction in the germline. (A) Fluorescence intensities of GFP-H2B (green) and mCherry-H2B (red) from pachytene-stage germ cells expressing H2B-2FPs. FLIM (right) images of H2B-2FPs pachytene-stage cells. The spatial distribution of the mean

fluorescence lifetime (τ) at each pixel is shown for wildtype (wt H2B-2FPs cells) (top) or set-2(bn129) H2B-2FPs mutant animals (bottom). Fluorescence lifetime values ranging between 2.2-3 ns are represented using a continuous pseudo-color scale. Scale bars, 10 μ m. (B) Statistical analysis of the FRET efficiency relative to control (wt), presented as box-and-whisker plots. The mean FRET value is indicated by a cross in each box. **** $p < 0.0001$ (two-tailed unpaired t test). (C) Relative fraction of FRET populations (sub-low, low, intermediate, and high) as defined previously (43) from wt and set-2(bn129) pachytene nuclei. * $p < 0.05$; (two-tailed unpaired t test); n.s, non-significant. n=5 gonads (approx. 350 nuclei) for wt, n=6 gonads (approx. 430 nuclei) for set-2(bn129).

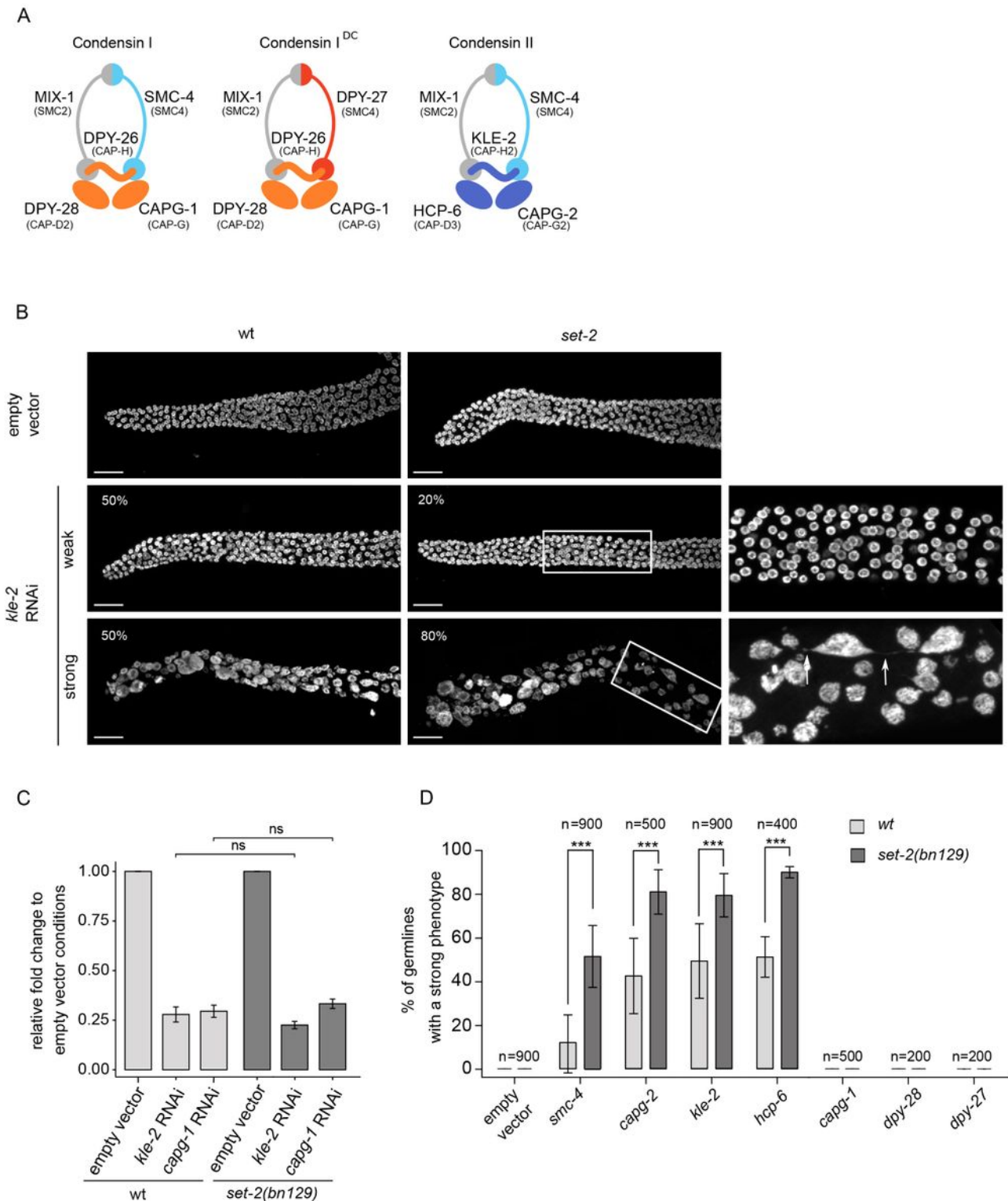


Figure 2

873 Figure 2. *set-2* inactivation enhances condensin-II depletion phenotypes. (A) *C. elegans* condensin subunits and their vertebrate homologs. (B) Confocal images of distal germline region from wildtype and *set-2(bn129)* animals treated with empty vector or *kle-2* RNAi. Representative images show examples of "wildtype-like" and "strong" phenotypes, with their presence indicated as percentage (%) of total (n=900, from 9 independent biological replicates) (scale bar, 20 μm). Arrow indicates the presence of chromatin

bridge (scale bar, 10 μm). Images correspond to a Max intensity projection using Fiji. (C) *kle-2* and *capg-1* mRNA levels in wildtype and *set-2(bn129)* mutant animals after RNAi 879 directed against the respective genes. Relative fold change was calculated with respect to empty vector 880 condition, following normalization with *pmp-3* and *cdc-42*. [*] $p < 0.05$ t-test. (D) Percentage of 881 germlines with "strong" phenotype after RNAi directed against condensin-II (*smc-4*, *capg-2*, *kle-2* and 882 *hcp-6*), condensins-I (*capg-1*, *dpy-28*) and condensin-IDC (*dpy-27*) in wildtype or *set-2(bn129)* mutants. 883 n= number of animals scored from 9 independent experiments for *smc-4* and *kle-2*, 4 for *hcp-6*, and 5 884 for *capg-1* and *capg-2*, and 2 for *dpy-28* and *dpy-27*. All scoring was performed in blind. [***] $p < 0.001$ 885 (t-test).

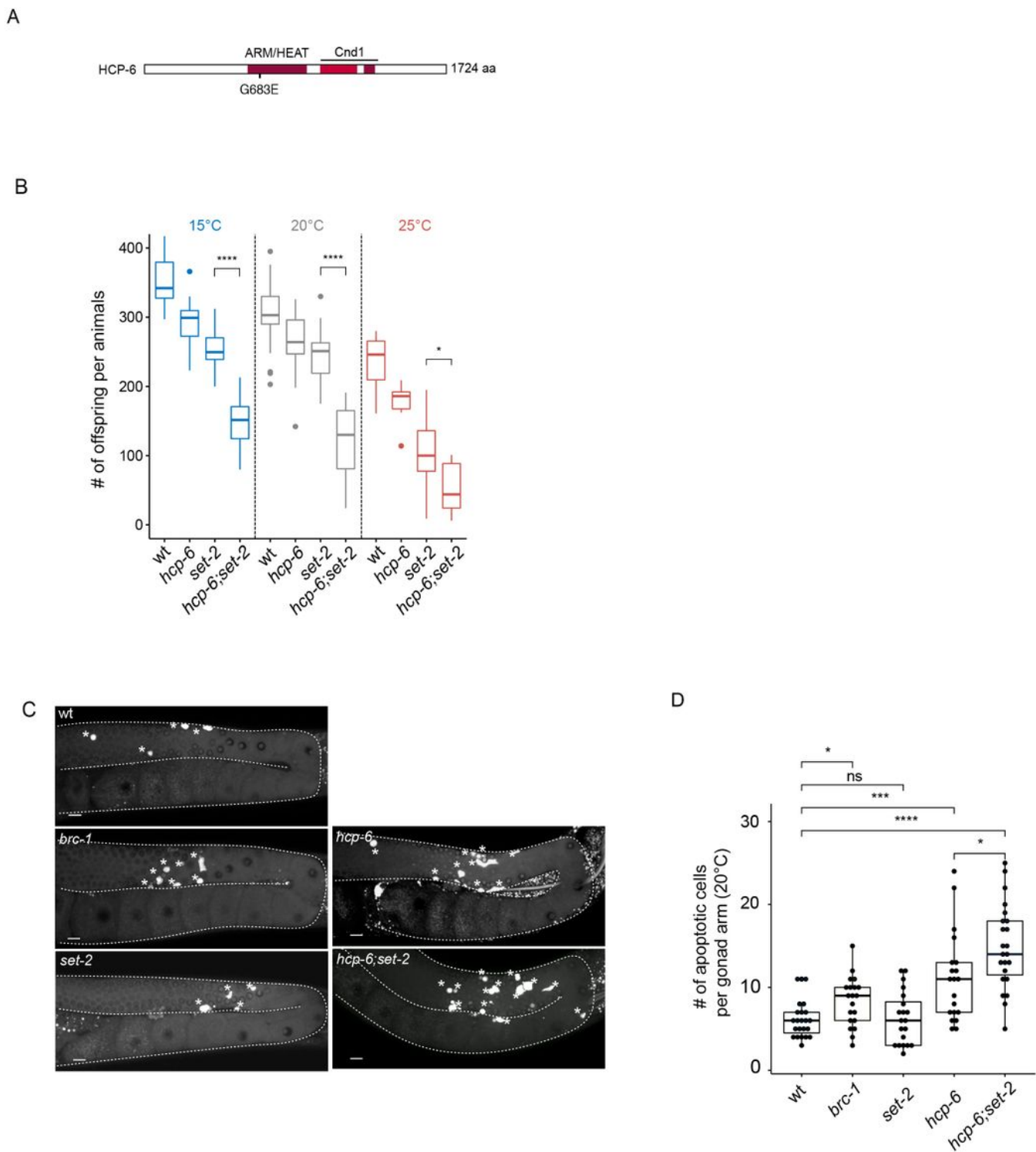


Figure 3

888 Figure 3. Enhancement of *hcp-6*(mr17) phenotypes in *set-2*(bn129) mutant animals. (A) Schematic
 889 diagram of HCP-6 protein and position of the mr17 mutation. Conserved ARM/HEAT and Cnd1
 890 (Condensin complex subunit 1) domains are highlighted in red. (B) Brood size per animals at indicated
 891 temperatures (15°C, 20°, 25°C), (n=11 animals per genotypes at 15°C and 25°C, and 33 at 20°C). [***]
 892 $p < 0.001$, [*] < 0.05 (t-test adjusted for multiple comparison with the Bonferroni method). (C) 893

Representative confocal images of germlines stained by orange acridine. Asterisks indicate apoptotic 894 cells. (D) quantification of the number of apoptotic cells in the germline of animals switched at 20°C 895 for 24h (n>20 gonads per genotypes). A Wilcoxon test was performed after a significant differences with 896 a Kruskal Wallis test, [ns] non significant difference, [*] p <0.05, [***] p <0.001, [****] p <0.0001.

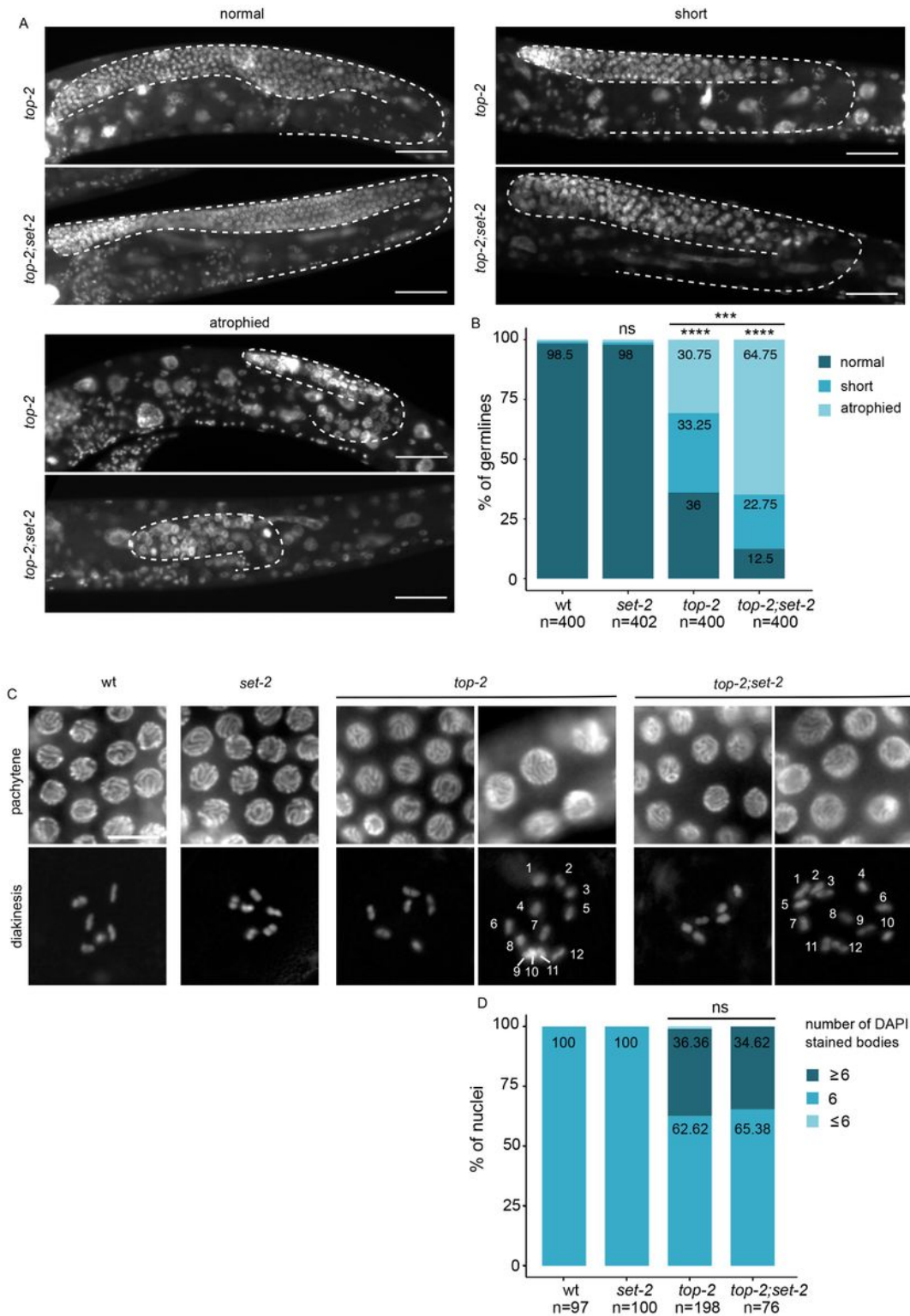
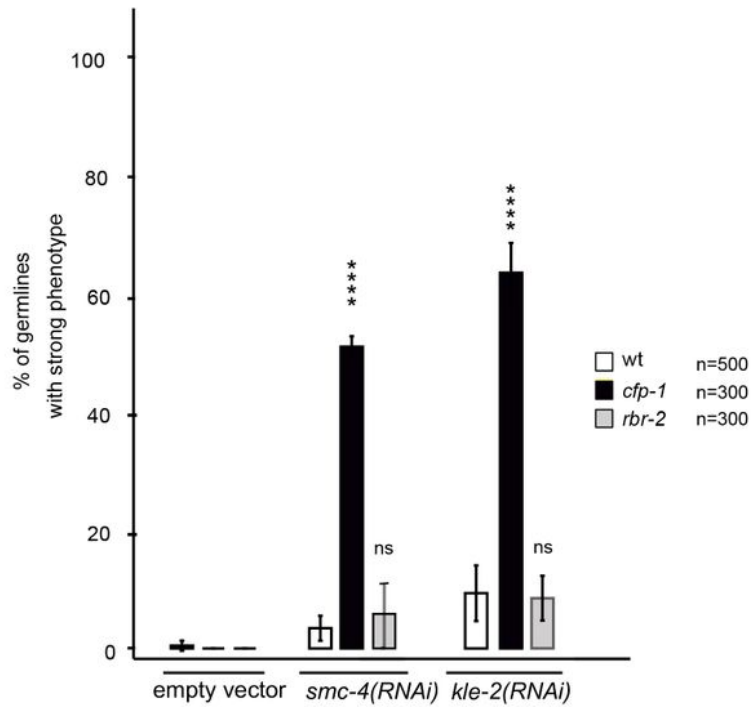


Figure 4

898 Figure 4. Enhancement of the top-2 mutant phenotype in absence of set-2. (A) Representative 899
images of DAPI stained adult germlines showing different phenotypic classes. (Scale bar, 10 μ m). (B) 900
Scoring of phenotypic classes. Animals were shifted to 24°C at the L1 stage and allowed to develop to
901 adulthood. Germlines categories are as defined in Materials and Methods. **** $p < 0.0001$, *** $p < 0.001$
902 significant difference between mutant backgrounds using chi-square test and FDR correction (ns:
non- 903 significant). Scale bar, 50 μ m. (C) Enlargement of pachytene and diakinetetic nuclei from wildtype
or 904 mutant animals. For top-2 single and top-2;set-2 double mutants, representative nuclei from normal
905 (left) and short (right) germlines are shown. Nuclei containing more than 6 DAPI stained bodies were
30 906 observed in both "short" and "normal" germlines. (D) Scoring of aneuploid nuclei from cells in 907
diakinesis (Scale bar, 10 μ m).

A



B

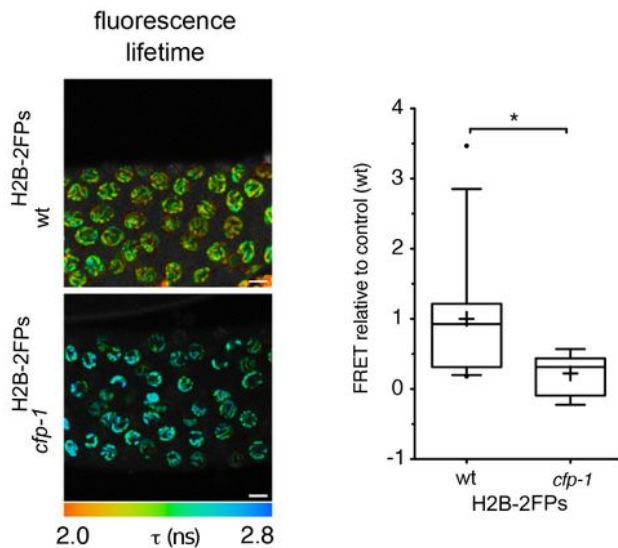


Figure 5

. Inactivation of COMPASS targeting component *cfp-1* mimics *set-2* inactivation. (A) 910 Percentage of germlines with "strong" phenotype after RNAi directed against condensin-II (*smc-4* or 911 *kle-2*) in wildtype, *cfp-1*(tm6369) and *rbr-2*(tm1231) mutants. n= number of animals scored from at 912 least 3 independent experiments. p <0.05, [***] p <0.001, [****] p <0.0001 (t-test); ns, not significant. 913 (B) Decreased chromatin compaction in *cfp-1* mutant germlines. Spatial distribution of the mean 914

fluorescence lifetime is shown for wildtype (wt H2B-2FPs) or *cfp-1* H2B-2FPs mutant animals. Fluorescence lifetime values (ns) ranging from 2.0 ns to 2.8 ns are represented using a continuous pseudo-color scale. Scale bars, 10 μ m. Statistical analysis of the FRET efficiency relative to control wt is presented as box- and-whisker plots. Mean FRET value is indicated by a cross in each box. * $p < 0.05$ (two-tailed unpaired t test). $n=13$ gonads for wt, $n=11$ gonads for *cfp-1*.

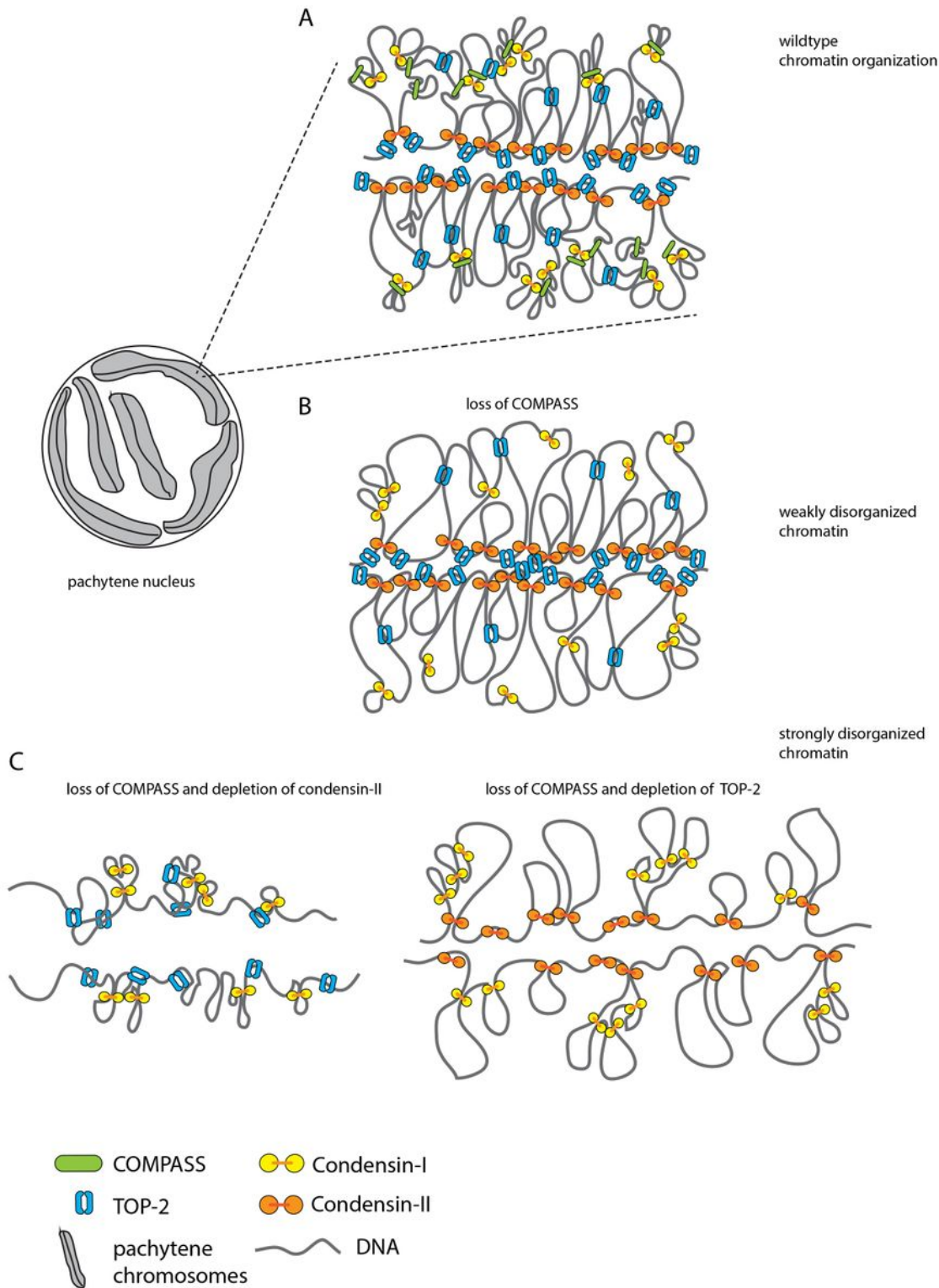


Figure 6

. Working model for cooperation between COMPASS, condensin-II and TOP-2 in 921 chromosome organization. In wild type, proper chromosome compaction results from the activity of 922 condensin-I (connected yellow circles), condensin-II (connected orange circles) and TOP-2 (blue broken 923 ring). The concerted action of condensins results in the formation of arrays of helical loops, with 924 condensin-II generating outer loops and condensin-I forming inner loops (80). TOP-2 may contribute to 925 compaction by modulating chromatin loops (60), or actively introducing self-entanglement in DNA 926 (32). COMPASS may mediate interactions between loops, possibly by contributing to the clustering of 927 transcribed loci (110). The absence of COMPASS results in subtle defects in chromosome organization 928 (weakly disorganized chromatin), but overall chromosome architecture is maintained by the action of 929 condensins, TOP-2 and additional proteins. Partial depletion of condensin-II or TOP-2 in the absence of 930 COMPASS results in cumulative defects in chromosome organization.

Supplementary Files

This is a list of supplementary files associated with this preprint. Click to download.

- [TableS1.xls](#)
- [FiguresS1S5.pdf](#)